The Astronomical Journal, 171:169 (19pp), 2026 March https://doi.org/10.3847/1538-3881/ae3e52
© 2026. The Author(s). Published by the American Astronomical Society.
OPEN ACCESS

Analysis of Karin and Koronis2 Asteroid Families: New Findings and Challenges

David Vokrouhlický[1], David Nesvorný[2], and William F. Bottke[2]
[1] Astronomical Institute, Charles University, V Holešovičkách 2, CZ 18000, Prague 8, Czechia; vokrouhl@cesnet.cz
[2] Department of Space Studies, Southwest Research Institute, 1301 Walnut Street, Suite 400, Boulder, CO 80302, USA
Received 2025 December 18; revised 2026 January 22; accepted 2026 January 25; published 2026 February 18

Abstract

We use our home catalog of the asteroid proper elements to study the Karin family. The hierarchical clustering method provides formal identification with 3863 members, but this set also includes objects from the neighboring Koronis2 and Kuitaisi families, as well as interlopers originating from the much older Koronis family. By tracking the trajectories of cluster objects backward in time, we identified 2161 asteroids whose orbits converged with that of their parent body (832) Karin at 5.72 ± 0.09 Mya (95% C.L.). This method of calculating the family's age is based on a novel convergence metric that is directly related to the velocities at which fragments were ejected from (832) Karin. We analyze the extent to which members $\leqslant$1.5 km in diameter had drifted in semimajor axis due to Yarkovsky thermal forces and find it reflects the tilt of their rotation poles away from the ecliptic, recording the influence of the YORP torque. Karin's size frequency distribution in the $\simeq$(0.8–3) km range follows a power law with a cumulative slope index -3.20 ± 0.01. Removing members of the Karin family from the original group, we examine the Koronis2 family, whose members are associated with (158) Koronis. We find it difficult for large members of the Koronis2 family to converge with the orbit of (158) Koronis within its previously estimated age of 7.6 Myr. Achieving such convergence would require the Koronis2 family to be older than 10 Myr, but our result must be verified with a direct numerical approach in the future.

Unified Astronomy Thesaurus concepts: Asteroids (72)

1. Introduction

The main asteroid belt contains several hundred clusters of collisional origin (e.g., A. Milani et al. 2014; D. Nesvorný et al. 2015; B. Novaković et al. 2022; D. Nesvorný et al. 2024a). For the most part, they have been identified in proper elements space, defined by semimajor axis a, eccentricity e, and sine of inclination $\sin I$, using the hierarchical clustering method (HCM) developed in the early 1990s (e.g., V. Zappalà et al. 1990; D. Nesvorný et al. 2015). Although powerful, the HCM approach often combines fragments from a given collisional event with nearby background asteroids or, as in the case of our work, with nearby families (e.g., A. Milani et al. 2014; B. Novaković et al. 2022). In such cases, further analysis is required to distinguish and isolate the substructures from one another. Spectroscopic or albedo information may be useful in this respect (e.g., J. R. Masiero et al. 2015; D. Nesvorný et al. 2015), but if the background population or overlapping families share the same physical characteristics, other tools are needed. In certain situations, the age of a family can serve as a distinguishing factor. Within this context, the Karin family represents an archetype of this class (with further examples such as the similarly young collisional cluster around the outer main belt active asteroid 300163 (2006 VW139) embodied in the Themis family; e.g., B. Novaković et al. 2012).

The discovery of the Karin asteroid family by D. Nesvorný et al. (2002a) marked the beginning of a new era in the century-long study of collisionally formed clusters within the main belt. For the first time, the epoch of the family's origin was determined through the direct backward propagation of its members' orbits. The success of this approach was the result of a fortunate combination of several factors unique to the Karin family: (i) its relatively young age of $\simeq$5.8 Myr, (ii) its position within one of the most dynamically stable orbital zones in the asteroid main belt, and (iii) the relatively large size of its parent body, measuring $\simeq$33 km in diameter, which produced a sufficient number of multikilometer-sized fragments. Since its discovery, the Karin family has been revisited numerous times (e.g., D. Nesvorný et al. 2003; D. Nesvorný & W. F. Bottke 2004; D. Nesvorný et al. 2006a, 2006b; V. Carruba et al. 2016), with each study uncovering new insights about this unique cluster. These findings have not only revealed previously unknown processes that can shape asteroid families but have also given us insights into whether young families are a plausible source for some meteorites.

In this study, we use the catalog of asteroid proper orbital elements by D. Nesvorný et al. (2024a) to investigate the Karin family.[3] This effort is especially timely given recent discoveries showing that the Karin orbital zone contains several other collisional clusters, such as the Koronis2 family associated with (158) Koronis, which are of significant scientific interest (see, e.g., L. A. Molnar & M. J. Haegert 2009; M. Brož et al. 2024; D. Nesvorný et al. 2024a, 2026).

In the case of young families, defined here as those approximately younger than 10 Myr old, the initial orbital configuration may be reached by propagating the heliocentric orbits of individual members backward in time. The most computationally demanding approach involves the backward integration of heliocentric osculating orbits (or heliocentric positions and velocities). In the Appendix, we present a novel method for characterizing a family's origin using mean orbital elements and then apply it to the Karin family. However, this

Original content from this work may be used under the terms of the Creative Commons Attribution 4.0 licence. Any further distribution of this work must maintain attribution to the author(s) and the title of the work, journal citation and DOI.

[3] Very similar results would have been obtained with the proper orbital elements available at the Asteroid Families Portal that currently contains as many inputs (see B. Novaković et al. 2022).

approach requires detailed backward numerical propagation of osculating orbits in the first place, and thus represents the same computer-time load.

As a first step, however, we find it more practical to employ a less complex method that reconstructs the past configuration of an asteroid family in a simpler orbital framework. In particular, we use the proper orbital element space (a, e, $\sin I$), extended by the proper values of the longitude of node Ω and perihelion ϖ. Although this set cannot capture the full details of each asteroid's orbital history, the use of this space does allow us to efficiently reconstruct the family's past orbital configuration with minimal computational demands (in particular, without having to perform new N-body integrations).

Given that the proper elements (a, e, $\sin I$) are already highly clustered and, by definition, remain constant over time (with the exception of semimajor axis a as discussed below), the primary focus of reconstruction lies in the behavior of proper Ω and ϖ. While their current values may appear randomly distributed between 0° and 360°, they must have been highly clustered at the time of the family's formation (see Section 3.1.3). Achieving convergence of these angles in a past epoch not only determines the age of the family but also enables us to identify and remove background asteroids and/or members of overlapping families.

The structure of our paper is as follows. In Section 2, we provide an overview of our method, which is fully applied to the state-of-the-art characterization of the Karin family in Section 3. In Section 3.1.3, we introduce a new approach to convergence analysis for young families, where the minimization function is directly linked to the velocity field with which the family members were initially dispersed after their parent body's disruption. We test this concept on the Karin family in the Appendix, though a comprehensive application of the method is left for future work. After isolating the true Karin family from the cluster identified by the HCM, we briefly examine the membership of the Koronis2 family within the remnant population (Section 3.2). While we highlight some intriguing puzzles associated with this important cluster (see also Section 3.3), we defer its detailed analysis to a separate study. Our findings are summarized in the concluding Section 4.

2. Methods

The process of determining the age of a family using the past orbital convergence of its members can be summarized as follows (for more details, see D. Nesvorný & W. F. Bottke 2004; V. Carruba et al. 2016). Consider a set of $N + 1$ asteroids that are candidate members of the family under study (either the Karin or Koronis2 family in this work). Each asteroid is assigned an index j, where $j = 0$ represents the reference body (the largest remnant in the family), and $j = 1, \ldots, N$ correspond to the remaining asteroids, typically ordered by increasing absolute magnitude H (or equivalently, decreasing size D).

We outline the procedure using the proper longitude of the ascending node, Ω_j, although the same process applies to the proper longitude of perihelion, ϖ_j. The current difference in proper longitude between each asteroid and the reference body is denoted as $\Delta\Omega_j(0) = \Omega_j(0) - \Omega_0(0)$. These values are randomly distributed throughout the definition interval. To project $\Delta\Omega_j$ back to a past epoch T (with T being positive in our notation), we utilize the associated proper frequencies, s_j and s_0, which are provided alongside the proper elements. This process allows us to assess the degree of orbital convergence at earlier times. From that, we have $\Delta\Omega_j(T) = \Delta\Omega_j(0) + (s_0 - s_j)\,T$ (the order of s frequencies in the bracket of the second term is reversed because a positive time T represents the past history).

A complication for observed families, however, is that the orbits of kilometer-sized asteroids are perturbed by thermal accelerations known as the Yarkovsky effect (e.g., D. Vokrouhlický et al. 2015). The primary secular effect pertains to the semimajor axis a, for which we approximate a linear change over time as a first-order assumption, i.e., $a_j(T) = a_j(0) - \dot{a}_j\,T$. The rate of change, $\dot{a}_j$, is unique to each asteroid and depends primarily on its size and the obliquity of its spin axis (negative for retrograde-rotating asteroids and positive for prograde-rotating asteroids; see D. Vokrouhlický et al. 2015). We neglect the small proper eccentricity and inclination changes caused by the Yarkovsky effect. Over timescales of <10 Myr, the semimajor axis changes by a negligible amount, even for kilometer-sized objects in the Karin/Koronis2 region, and as such, $a_j(T)$ is not used as the primary metric for orbital convergence. Instead, the focus is on the indirect effect this change has on proper frequencies (such as s_j), which are highly sensitive to variations in a_j and play a dominant role in the analysis (e.g., D. Nesvorný & W. F. Bottke 2004). The nodal difference $\Delta\Omega_j(T)$ must therefore account for the effect of changes in the semimajor axis and can be expressed as:

$$\Delta\Omega_j(T) = \Delta\Omega_j(0) + (s_0 - s_j)\,T + \frac{1}{2}\left[\left(\frac{\partial s}{\partial a}\right)_j \dot{a}_j - \left(\frac{\partial s}{\partial a}\right)_0 \dot{a}_0\right] T^2. \quad (1)$$

In principle, higher-order derivatives of s with respect to a should appear in the right-hand side of Equation (1), but their values are small and may be neglected for $T < 10$ Myr. The first derivatives, however, must be known from analytical formulations or from estimates based on numerical analysis. We took the second option and found that a constant value $(\partial s/\partial a) = -69\farcs0 \pm 1\farcs3\ \mathrm{yr}^{-1}$ provides an adequate approximation for our purposes, with the uncertainty reflecting the range of values inferred in the Karin family region. Similarly, for the proper perihelion frequency g, we found that $(\partial g/\partial a) = 85\farcs6 \pm 3\farcs7\ \mathrm{yr}^{-1}$ offers a satisfactory approximation, which we apply to all asteroids within the Karin orbital space.

Combining the above formulation for Ω_j with that of ϖ_j, we define a target function $\mathcal{C}(T)$ to characterize the degree of convergence of the proper secular angles at any past epoch T analyzed in the simulation.

$$\mathcal{C}^2(T) = \mathcal{C}_\Omega^2(T) + \mathcal{C}_\varpi^2(T) = \sum_{j=1}^{N} [\Delta\Omega_j^2(T) + \Delta\varpi_j^2(T)], \quad (2)$$

where the summation includes all family fragments, beginning with the second-largest remnant. The parts $\mathcal{C}_\Omega$ and $\mathcal{C}_\varpi$ in $\mathcal{C}$ denote individual contributions from the convergence of the nodes and perihelia.

We also define averages $\mathcal{C}'^2 = \mathcal{C}^2/(2N)$, $\mathcal{C}_\Omega{}'^2 = \mathcal{C}_\Omega^2/N$ and $\mathcal{C}_\varpi{}'^2 = \mathcal{C}_\varpi^2/N$. The uniformly distributed angles $\Delta\Omega_j$ and $\Delta\varpi_j$ would have $\mathcal{C}' = 180°/\sqrt{3} \simeq 104°$. In contrast, at the formation of the Karin or Koronis2 families, we expect $\mathcal{C}' \simeq 1° - 2°$ (Section 3.1.3).

The goal of the initial family reconstruction method is to seek an epoch T in the past such that $\mathcal{C}'$ in (2) with $\Delta\Omega_j(T)$ substituted from (1), and similarly for perihelia differences, collapses to the expected degree-level. Some candidate asteroids from the originally analyzed sample may have secular angles that fail to converge at the epoch where the majority converge. These are interlopers that must be iteratively removed from the list. As with most optimization problems, the solution is achieved by adjusting a set of free parameters. In our case, we consider the a priori unknown drift rates $\dot{a}_j$. Interestingly, their fitted values can be independently verified a posteriori through observations, particularly by analyzing photometric data to determine the rotation states of the asteroids.

3. Results

We utilized our home catalog of asteroid proper orbital elements from D. Nesvorný et al. (2024a) to identify the Karin family using the HCM with a 10 m s^{-1} cutoff velocity (the order of magnitude by which the currently observed Karin members are separated from (832) Karin; e.g., D. Nesvorný et al. 2006a). The resulting cluster comprises 3863 objects, which include members of both the Karin and Koronis2 families, as well as potential interlopers from the older Koronis family and the younger Kuitaisi/Koronis3 families. Notably, the same cluster is obtained when starting the HCM method from (158) Koronis and applying the same velocity cutoff. This result stems from the overlap between the two families.

In the following analysis, we apply the methods outlined in Section 2 to separate the Karin and Koronis2 families from the identified asteroid cluster. We first focus on identifying the Karin family, given that it is well established, it has a younger age, and that it has well-constrained properties (Section 3.1). Once the Karin members are removed from this cluster, we will analyze the remaining asteroid sample to identify the members of the Koronis2 family (Section 3.2).

3.1. Karin Family

3.1.1. Step 1: Analysis of Large Member Population

Since its discovery in 2002 (D. Nesvorný et al. 2002a), the population of large members within the Karin family has been extensively studied. The main results relevant for our work are as follows:

1. The physical parameters of the largest family member (832) Karin are well determined: (i) its size is 16.3 km, based on an analysis of Wide-field Infrared Survey Explorer (WISE) observations (e.g., J. R. Masiero et al. 2011), and (ii) its slow rotation period of 18.35 hr and pole obliquity of 42° were both constrained by analysis of photometric observations (e.g., S. M. Slivan & L. A. Molnar 2012). Using this information, and assuming it has a 2.5 g cm^{-3} bulk density, which is typical for S-type asteroids of this size (e.g., D. J. Scheeres et al. 2015), we estimate that its Yarkovsky drift rate is $\dot{a}_0 \simeq 1.2 \times 10^{-5}$ au My^{-1}. This value will be used in all of the simulations discussed in this paper.
2. The past orbital convergence of Karin's large members yielded a unique age solution for the Karin family, namely $T = 5.75 \pm 0.05$ Myr by D. Nesvorný & W. F. Bottke (2004) or $T = 5.75 \pm 0.01$ Myr by V. Carruba et al. (2016). The uncertainty of the latter should be taken as a formal one; a more realistic value would likely be an order of magnitude larger.
3. The hydrocode simulations of the impact event that formed the Karin family, conducted by D. Nesvorný et al. (2006a) and calibrated based on their success in reproducing the size distribution of the largest members, predict that the mean ejection velocity for $D \geqslant 3$ km size fragments was about 10 m s^{-1}. It reached values larger than 30 m s^{-1} for kilometer-sized fragments.

To ensure a robust analysis, we began by focusing on a population of large asteroids among the 3863 objects identified as members of the Karin cluster by the HCM. Specifically, we selected all objects with an absolute magnitude of $H \leqslant 16.7$, corresponding to a size of approximately 1.3 km assuming a geometric albedo of 0.23. This initial selection resulted in 646 asteroids.

To refine the sample further, we excluded objects located significantly beyond the well-defined boundaries of the Karin family in 2D planes defined by (i) a and proper e orbital elements, and (ii) proper a and absolute magnitude H. After this step, we narrowed the sample down to 421 candidate members of the Karin family, including the asteroid (832) Karin, within the chosen H limit.

Next, we applied the method described in Section 2 to search for convergence of the proper nodes Ω and perihelia ϖ within the past 10 Myr interval of time. In order to infer a possible range of semimajor axis drift rates $\dot{a}$ for each of the asteroids (except 832 Karin), we assigned them a size D by either (i) directly obtaining the information from the database provided by WISE (J. R. Masiero et al. 2011) or (ii) assuming the objects had a $p_V = 0.23$ geometric albedo, the median value for the Koronis family as determined from WISE observations (e.g., J. R. Masiero et al. 2013). There were 24 cases in the first group.

We then used the linearized theory of heat conduction for spherical bodies from D. Vokrouhlický (1998) to estimate the maximum possible values of $\dot{a}_{\max}$. Note that for an individual body, $\dot{a}_{\max}$ also depends on the rotation period P and the thermal inertia of the surface Γ. Given that we do not know these values for our candidate objects at this time, we assumed $\dot{a}_{\max}$ reached its maximum over all possible values of (P, Γ). This calculation yielded $\dot{a}_{\max} = \pm 3.1 \times 10^{-4}/D$ au My^{-1}, where D is in kilometers, and the positive and negative values are for the two extreme obliquities of 0° or 180°, respectively. For each object in the sample of 420 Karin-family candidates, we considered $\dot{a}$ within these limits.

Proceeding with 0.01 Myr time steps in T, we found the minimum possible values of $\Delta\Omega_j(T)$ and $\Delta\varpi_j(T)$ and subsequently calculated $\mathcal{C}(T)$ for the entire sample. At the epoch corresponding to the $\mathcal{C}(T)$ minimum, we evaluated the contributions of each asteroid in the sample and identified those with contributions exceeding 4 times the minimum value as interlopers. These nonconverging objects, defined as interlopers, were subsequently removed from the sample. The process was iteratively repeated until no additional interlopers were detected. This refinement resulted in a final selection of 370 Karin family members that are smaller than (832) Karin but larger than 1.3 km (namely $H \leqslant 16.7$ from our initial selection). The number of removed objects, 49 out of 420 (832 Karin not counted), roughly informs us about the fraction

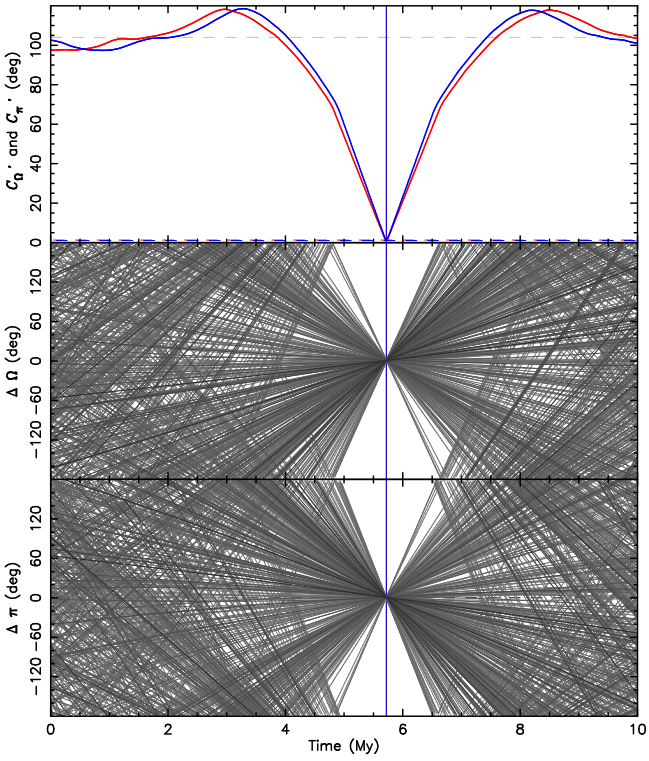

Figure 1. Convergence of the proper longitude of node (middle panel) and perihelion (bottom panel) of 370 Karin family members with $H \leqslant 16.7$ at $T = 5.72$ Myr. Darker lines for larger members. The top panel shows behavior of $\mathcal{C}'_\Omega$ (red) and $\mathcal{C}'_\varpi$ (blue) defined in (1). Both show sharp minima at nearly the same epoch, as required by a satisfactory global solution of $\mathcal{C}$, attaining the best-fit values $1\overset{\circ}{.}29$ for nodes and $1\overset{\circ}{.}05$ for perihelia. The gray dashed level at the top panel corresponds to $\mathcal{C}'$ value of a uniform distribution for comparison.

of interlopers in the Karin family, namely $\simeq$11% (most of which come from the Koronis2 and Kutaissi clusters).

Figure 1 shows the successful convergence of proper nodes and perihelia toward the orbit of (832) Karin, while the middle panel shows $\Delta\Omega$ values, and the lower panel shows $\Delta\varpi$ values. To verify that the convergence of both elements occurs at the same epoch, we split $\mathcal{C}'(T)$ into the two components $\mathcal{C}'_\Omega(T)$ (red curve) and $\mathcal{C}'_\varpi(T)$ (blue curve) in the top panel. Their minimum values, $1\overset{\circ}{.}29$ for the nodes and $1\overset{\circ}{.}05$ for the perihelia, indeed occur simultaneously at $T = 5.72$ Myr.

To analyze the behavior of the composite function $\mathcal{C}'(T)$ near its minimum and to estimate the age of the Karin family using our method, we consider the information shown in Figure 2. At first sight, an inconsistency appears between $\mathcal{C}'_\Omega(T)$ and $\mathcal{C}'_\varpi(T)$ in the top panel of Figure 1 and substantially shallower-in-time $\mathcal{C}'(T)$ in Figure 2. In Figure 1, however, we considered fixed values of $\dot{a}_j$, namely those that resulted in the best convergence solution, and hold them to compute $\Delta\Omega$ and $\Delta\varpi$ in other epochs. In contrast, in Figure 2, at each epoch T, we allowed the values $\dot{a}_j$ to vary so that the smallest value $\mathcal{C}'(T)$ is locally reached. These values are different at each time. This indicates that a much better convergence is achieved over a broader range of epochs near the global minimum at $T = 5.72$ Myr in Figure 2 than in Figure 1.

To establish a limit on the individual values within $\mathcal{C}'(T)$ that could provide a confidence interval for the possible age of the Karin family, we formally assume an uncertainty of approximately $\simeq 1\overset{\circ}{.}5$ in both $\Delta\Omega_j$ and $\Delta\varpi_j$. This level reflects

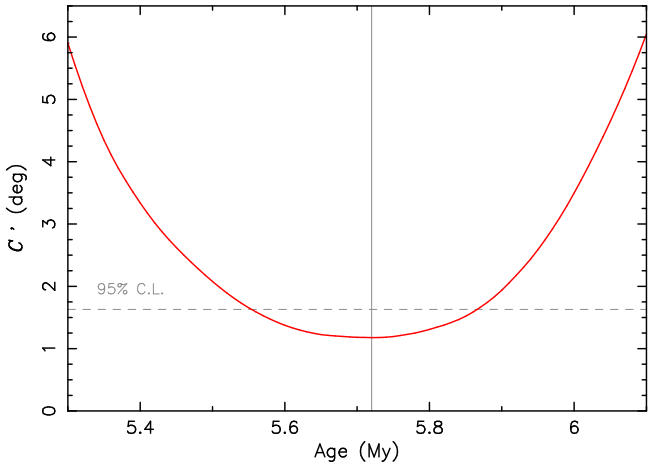

Figure 2. Behavior of the target function $\mathcal{C}'$ near its minimum at $T = 5.72$ Myr (vertical gray line) combining convergence of proper nodes and perihelia of 370 Karin family members with $H \leqslant 16.7$. The dashed gray horizontal line indicates the 95% confidence level of the age solution assuming $\mathcal{C}'$ represents a merit function of minimization procedure with $\simeq 1\overset{\circ}{.}5$ uncertainty of the $\Delta\Omega_j$ and $\Delta\varpi_j$ values (each characterized by normal distribution; see W. H. Press et al. 2007).

the previously mentioned ejection velocities of large Karin fragments, as well as the noise introduced by perturbations from massive bodies in the main belt (see the Appendix and Figure 15).

Assuming a Gaussian distribution for both angles and considering 370 degrees of freedom by adjusting the values of $\dot{a}_j$ for each asteroid, we can set a $\mathcal{C}'(T)$ threshold for every chosen confidence limit (C.L.) in the age solution (see W. H. Press et al. 2007). For 95% C.L., we obtained the value shown by the dashed horizontal line in Figure 2. This translates to the Karin age of $T = 5.72^{+0.16}_{-0.19}$ Myr based on our method.

Before proceeding further, we took a closer look at the largest asteroids within the converging sample. We found three bodies, (7719) 1997 GT36, with $D = 4.7 \pm 0.5$ km, (33143) 1998 DJ7, with $D = 3.6 \pm 0.7$ km, and (40510) 1999 RU87, with $D \simeq 3.1$ km, all of which have $\sin I > 0.0374$. While the Karin family stretches over a large set of proper inclination values, a distinct feature of the Koronis2 family is its tight confinement in proper inclination values between 0.0374 and 0.0378 (e.g., L. A. Molnar & M. J. Haegert 2009; M. Brož et al. 2024). Interestingly, while these three asteroids converge to (832) Karin, they also converge to (158) Koronis, as shown in Section 3.2. Unlike the other objects in the initial sample of bodies with $H \leqslant 16.7$ selected in this section, their convergence to either of the two largest remnants in the Karin and Koronis2 families does not provide definitive evidence regarding their membership in one family or the other. In this situation, we adopted a conservative approach and excluded them from the Karin family (though we acknowledge that readers holding an opposing view may prefer to retain them as Karin family members). As a result, we are left with 367 members in the Karin family with $H \leqslant 16.7$ (in addition to (832) Karin itself).

The remarkable 1° level of convergence in both nodes and perihelia, as demonstrated above, stems from the adjustment of the mean drift rates $\dot{a}_j$ for each body. Figure 3 displays these values for all 367 converging asteroids in our nominal Karin family, along with the three discarded asteroids (7719, 33143,

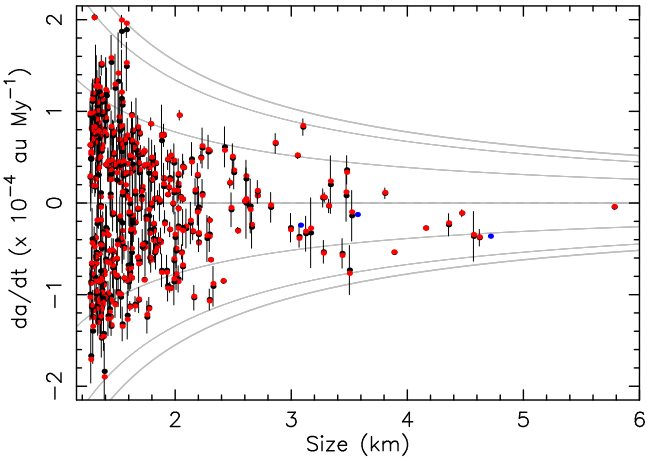

Figure 3. Adjusted values of mean semimajor axis drift-rate values $\dot{a}$ for 367 Karin family members with $H \leqslant 16.7$ as a function of their size D. Red symbols correspond to the solution with minimum dispersion of the secular angles expressed by $\mathcal{C}$ function in (2). The black symbols, and vertical bars, are the mean and standard deviation of their distribution from solutions with T sampling the 95% C.L. interval of Karin family ages, namely between 5.53 and 5.88 Myr (Figure 2). The enveloping thick gray lines are the estimated maximum values $\dot{a}_{\max} = \pm 3.1 \times 10^{-4}/D$ au My^{-1} from the linearized heat conduction model on spherical bodies and bulk density of 2.5 g cm^{-3} (e.g., D. Vokrouhlický 1998). The positive and negative maximum values correspond to 0° and 180° obliquity. The thin gray lines are for intermediate obliquity values incremented by 30°. For sake of completeness, we also displayed the $\dot{a}$ values corresponding to 7719, 33143, and 40510 (blue symbols), whose membership in Karin or Koronis2 families is ambiguous (see Section 3.1).

and 40510), plotted as a function of their estimated size D: the red symbols represent their solutions corresponding to the minimum $\mathcal{C}'(T)$ value at $T = 5.72$ Myr, and (ii) the black symbols, with associated uncertainty intervals, represent their mean and standard deviation derived from individual best-fitting convergences with T across the 95% C.L. interval of Karin age values (Figure 2).

We may conclude that the $\dot{a}_j$ solution is robust, as the variations in their values are relatively small, and the best-fitting values consistently remain close to the mean obtained by sampling the uncertainty in the Karin age. Additionally, all $\dot{a}_j$ values fall within the range defined by $\dot{a}_{\max}$ for the estimated size. This indicates that that the allowed interval for $\dot{a}$ was even more generous than necessary. For Karin members with sizes between $\simeq$1.3 and 3.5 km, the $\dot{a}$ values are evenly distributed between positive and negative values, pointing to an isotropic distribution of their rotation poles.

Conversely, it has been previously observed that members with $D \geqslant 3.5$ km members consistently exhibit negative $\dot{a}$ values, indicating a predominantly retrograde sense of rotation (as noted in D. Nesvorný & W. F. Bottke 2004; V. Carruba et al. 2016). The hypothesis that they all have such values can be tested through photometric observations that can directly determine their rotation states. Such work could also provide important constraints for numerical models describing the disruption of the Karin family's parent body.

3.1.2. Step 2: Analysis of Small Member Population

In the next step, we consider the sample of 3217 asteroids with $H > 16.7$ in our original Karin cluster identified using HCM in proper element space. The set of Karin members with $H \leqslant 16.7$ precisely determines the family's age. We therefore

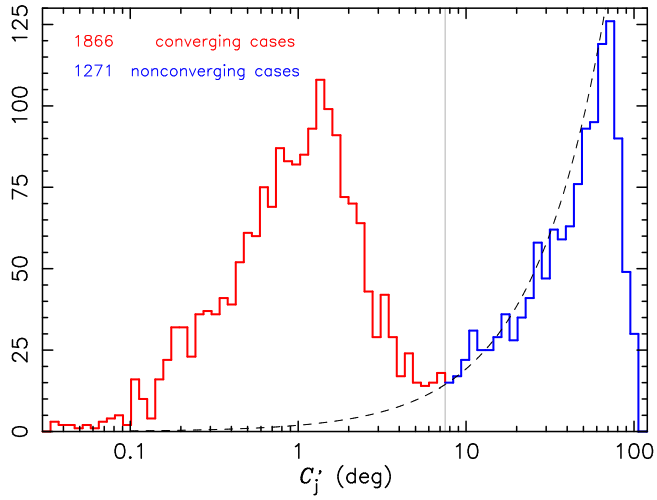

Figure 4. Differential distribution of $\mathcal{C}'_j = \sqrt{(\Delta\Omega_j^2 + \Delta\varpi_j^2)/2}$ values by which each of the 3217 small ($H > 16.7$) Karin family candidates contributes to the convergence target function (2) at fixed epoch $T = 5.72$ Myr. The distribution is clearly bimodal, with 1866 inputs having $\mathcal{C}'_j \leqslant 7\overset{\circ}{.}5$, for which we adopted a limit for satisfactory convergence (red segment); these asteroids define the population of small Karin members. The remaining 1217 objects do not exhibit satisfactory convergence to (832) Karin at the epoch of the Karin family formation (blue segment). Given the logarithmic binning at the abscissa, the dashed line characterizes a uniform distribution of $\mathcal{C}'_j$.

fixed the age at $T = 5.72$ Myr and focused on which of the 3217 small asteroids have the potential to converge to (832) Karin at the selected epoch in the past.

We use the same convergence method as described earlier, assigning each small asteroid a $\dot{a}_j$ value within the range of $\dot{a}_{\max} = \pm 3.1 \times 10^{-4}/D$ au My^{-1}. The only difference is that we use a slightly wider range due to the smaller sizes of the asteroids in the second candidate sample. The diameter D was estimated using the absolute magnitude H and a mean geometric albedo of $p_V = 0.23$. We did not follow an iterative process, as we anticipated that many of the objects in this sample would not converge with (832) Karin.

For each asteroid tested, we only optimized the value of $\dot{a}_j$ to reach the best convergence result, which we quantitatively express using a contribution $\mathcal{C}'_j{}^2 = (\Delta\Omega_j^2 + \Delta\varpi_j^2)/2$ in $\mathcal{C}^2$. We set the threshold for acceptable convergence at $\mathcal{C}'_j \leqslant 7\overset{\circ}{.}5$. We argue that this value provides a generous margin, considering the excellent level of convergence observed in the sample of larger Karin members.

Figure 4 shows the distribution of the resulting $\mathcal{C}'_j$ values for the entire sample. As expected, it has a bimodal nature, which allows us to separate small members of the Karin family (red segment of the distribution) from interlopers (many of which will contribute to the population of the Koronis2 family; blue segment of the distribution). The division of the two groups appears very close to our choice $\mathcal{C}'_j \leqslant 7\overset{\circ}{.}5$, which we consider to be a nice a posteriori justification for our assumption.

The median value of $\mathcal{C}'_j$ in the converging group is $1\overset{\circ}{.}02$, which is consistent with the value characterizing the convergence of the larger members of the Karin family (Section 3.1.1). The distribution of the $\mathcal{C}'_j$ values of Karin-unrelated asteroids appears to peak near 70°, but this is merely an artifact caused by the use of logarithmic binning in Figure 4. In reality, their distribution is uniform, as illustrated by the dashed line. When extrapolated to $\mathcal{C}'_j \leqslant 7\overset{\circ}{.}5$, along

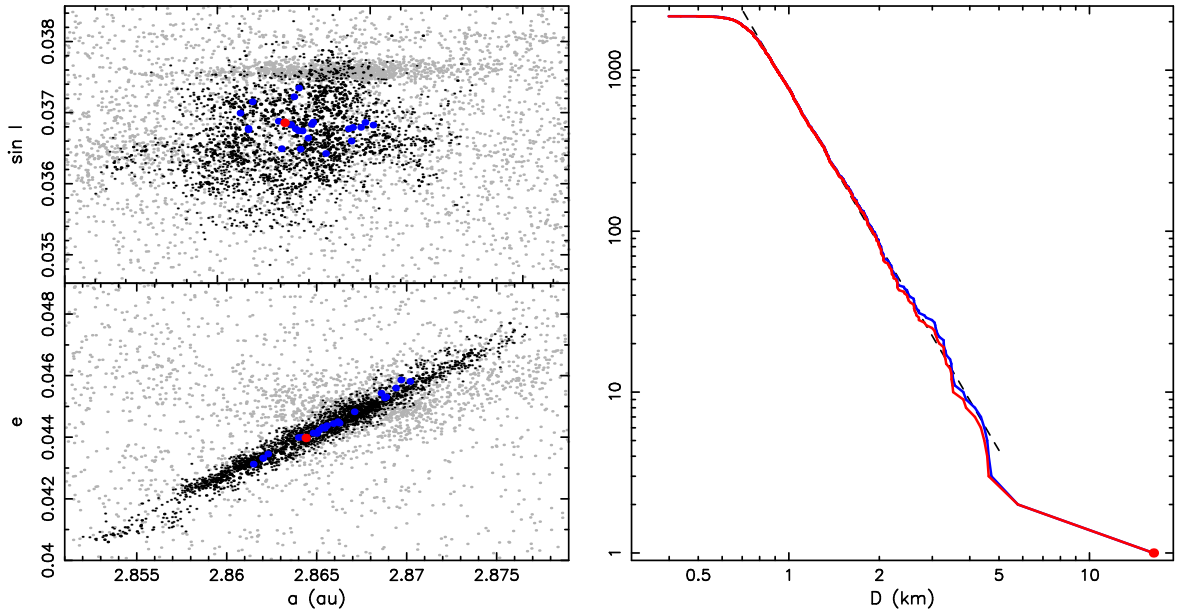

Figure 5. Left panels: Karin family members (black symbols) projected onto 2D planes of proper semimajor axis a at the abscissa, and proper sine of inclination $\sin I$ (top) and eccentricity e (bottom) at the ordinate. The largest body (832) Karin is shown by the red circle, and members with size $\geqslant$3 km are shown by blue symbols. The gray dots show unrelated background asteroids in the Koronis family, including the Koronis2 cluster (at $\sin I \simeq 0.0376$). Right panel: cumulative size distribution for 2161 members in our conservative identification of Karin family (red curve). Sizes are of the 21 largest objects from WISE observations, while those for the remaining members are determined from their absolute magnitude H and assumed albedo $p_V = 0.23$, a mean value of the Koronis family from WISE data as well (J. R. Masiero et al. 2011, 2013). In between 0.85 and 3 km, the distribution is fairly well matched by a power law $N(>D) \propto D^{-\alpha}$ with a slope index $\alpha = 3.2$ (dashed line). For the sake of comparison, we also show a distribution that would include asteroids 7719, 33143, and 40510 with an ambiguous membership in either Karin or Koronis2 families (see Section 3.1; blue curve).

with the presence of a tail of formally converging objects nearing the arbitrarily chosen separation threshold, this suggests that some asteroids in this group may still be interlopers from the background population or the Koronis2 family. We estimate that there could be several dozen to ~100 such interlopers.

To investigate further, we closely examined the orbits contributing to the "neck" region between the converging and nonconverging groups. We identified 73 asteroids that, based on their proper orbital elements, reside within a halo that is too distant from the core members of the Karin family. One particularly suspicious feature is their alignment in $\sin I$ near 0.0375, a value corresponding to the center of the Koronis2 family. For this reason, we decided to exclude these 73 asteroids from the Karin family. This refinement leaves us with 1793 confirmed Karin members with $H > 16.7$. Combined with the sample identified earlier in Section 3.1.1, the updated population of Karin family members, including (832) Karin, now totals 2161 asteroids.

The left panels in Figure 5 show the distribution of the identified members of the Karin family in the 2D projections of proper orbital elements: (i) (a, $\sin I$) (top), and (ii) (a, e) (bottom). A highly correlated diagonal distribution in the (a, e) projection, which is a distinct characteristic that played a key role in the family's initial discovery (D. Nesvorný et al. 2002a), strongly supports the idea that the parent body of the family was disrupted near the perihelion of its orbit. From a quantitative perspective, $|f_\star| \leqslant 30°$ from Equations (3) and (4), where $f_\star$ is the true anomaly of the parent body at the collision.

The right panel of Figure 5 shows the cumulative size frequency distribution (SFD) $N(>D)$ of the Karin family. Only 21 of the largest members have their sizes determined based on the analysis of WISE data. For the remaining asteroids, we assumed a geometric albedo of $p_V = 0.23$, the average value for the surrounding Koronis family (e.g., J. R. Masiero et al. 2013). The population of the largest members is too small to enable a meaningful fit of $N(>D)$ with a sufficiently smooth and simple function. However, within the size range of approximately 0.8 and 2.5 km, a power-law approximation $D(>D) \simeq D^{-\alpha}$ with $\alpha = 3.20 \pm 0.01$ provides an excellent fit. Below 0.8 km, the population is observationally incomplete.

We verified the 0.8 km threshold using well-characterized observations of the Catalina Sky Survey between 2016 and 2022, analyzed extensively by D. Nesvorný et al. (2024b). This led us to infer the completeness level as $H \simeq 17.2$. With our assumed albedo value, this translates to a size of approximately 1 km. This dataset presents an opportunity to revisit the modeling efforts of D. Nesvorný et al. (2006a) to gain a more detailed understanding of the disruption of the Karin family's parent body. For example, we may be able to more accurately constrain the size of the parent body, or we may now be able to better estimate the unseen mass of fragments below the completeness limit. Either advance could yield highly valuable insights (see the discussion in Section 4).

Figure 6 shows the adjusted drift rates $\dot{a}_j$ for the entire population of 2161 Karin family members. The data on small members presented in this section introduces notable differences compared to Figure 3. The information does not just change the number of data points. It instead also reveals the onset of new behavior for sizes $D \leqslant 1.1$ km. While for larger sizes, the $\dot{a}_j$ values are approximately evenly distributed across the entire admissible range of $\pm\dot{a}_{\max}$, the distribution for smaller sizes exhibits distinct characteristics: (i) it avoids very small drift rates, and (ii) it shows a preference for drift rates corresponding to rotation pole latitudes of $\pm 30°$.

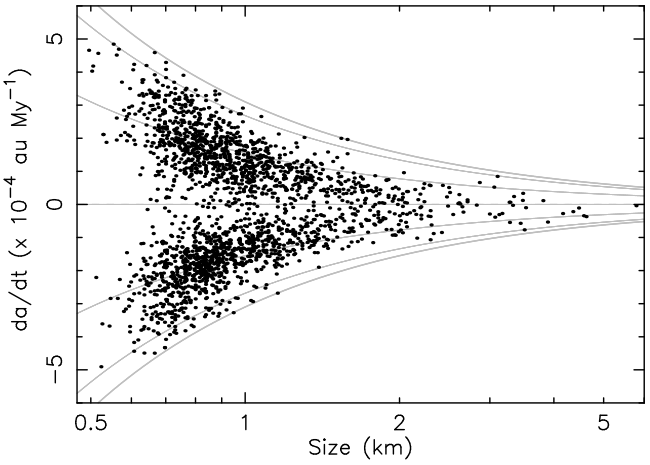

Figure 6. Mean values of the semimajor axis drift $\dot{a}$ (black symbols) of all 2160 members in the Karin family (except 832 Karin itself) inferred from convergence of their proper secular angles Ω and ϖ as a function of their size D. The gray lines are the same as in Figure 3. Below $\simeq$1.5 km size, the $\dot{a}$ values have a nonuniform distribution, avoiding zero value and having peaks at about half of the maximum value for both the prograde- and retrograde-rotation regime. This is due to the YORP effect that made rotation pole directions of subkilometer Karin members tilt away from the ecliptic plane (see V. Carruba et al. 2016).

This polarization in the drift rates of small Karin members was first identified and explained by V. Carruba et al. (2016) as a result of the obliquity changes driven by the Yarkovsky–O'Keefe–Radzievskii–Paddack (YORP) effect (for more details on the YORP effect, see, e.g., D. Vokrouhlický et al. 2015). In this work, the trend is confirmed using a much larger sample of asteroids and is further extended to even smaller sizes.

Finally, having achieved a very high level of convergence of the secular proper angles of all Karin members to (832) Karin at the epoch of the family's formation, we can now explore what additional details about the initial family configuration might still be uncovered. A straightforward approach is to project the other proper orbital elements backwards in time to their original values. However, there are some inherent limitations to this method. Specifically, we assume the proper eccentricities and inclinations remain constant, meaning their initial values are equal to their current ones. Yet, the proper semimajor axes involve a nontrivial, albeit simplified, adjustment, namely that their initial values are computed as $a_j(T) = a_j(0) - \dot{a}_j\, T$. This effect is small and has not been directly used so far.

The changes in the Karin family configuration within the 3D space of proper orbital elements (a, e, $\sin I$) are displayed in Figure 7. The present-day distribution is shown in the left panels, while the reconstruction of the initial configuration appears in the right panels. Interestingly, the differences are both significant and entirely consistent with expectations. In the (a, e) plane, the initial distribution becomes even more tightly aligned with the linear correlation. This further constrains the possible range of the parent body's true anomaly, $f_\star$ at the epoch of family formation, of being very close to the value $f_\star = 0°$. Similarly, notable changes are evident in the (a, $\sin I$) projection, where the Karin family fragments begin to form a filamentary structure, resembling a sharper, more focused version of the currently diffuse distribution.

Even more intriguingly, numerical simulations of the Karin family's breakup performed by D. Nesvorný et al. (2006a) predict the existence of such filamentary structures. This agreement between the theoretical predictions and our data-driven reconstruction appears to validate both approaches. Bridging the remaining gaps between the two methodologies represents an exciting direction for future work. Achieving this will likely require incorporating the past orbital dynamics of Karin family members, extending beyond the simplified model based solely on proper elements.

3.1.3. Step 3: Further Improvements?

The convergence of secular angles has been used as a standard method for estimating the age of very young asteroid families since the work of D. Nesvorný et al. (2002a). This approach, however, only represents a necessary condition for reconstructing the family configuration at its origin. The ultimate goal would be to align the full heliocentric state vectors of all family members together, namely, at their mutual distance defined by the Hill radius of the parent body and very small relative velocities. Yet, for families consisting of thousands of members and ages exceeding millions of years, achieving this level of reconstruction appears to be an unattainable task. So far, it has only been successfully achieved in the case of much younger asteroid pairs (e.g., D. Vokrouhlický & D. Nesvorný 2008).

Despite these challenges, it may still be possible to improve upon this method when applied to asteroid families such as the Karin family. In this section, we explore this possibility. Fully leveraging this novel approach necessitates transitioning from proper to mean orbital elements and replacing analytical techniques with numerical methods. The initial steps of this new methodology are discussed in greater detail in the Appendix.

The initial ejection velocities of Karin family members, as referenced to the largest remnant (832) Karin, may be expressed in its orbital plane using the radial, transverse, and out-of-plane components (V_r, V_t, V_z). To map these values into differences in orbital elements (specifically, the osculating orbital elements), we must also determine the argument of perihelion $\omega_\star$ and the true anomaly $f_\star$ of (832) Karin at the time of origin. Moreover, the resulting mathematical expressions become more straightforward by scaling the components (V_r, V_t, V_z) by the heliocentric orbital velocity $V_0 \simeq 17{,}600$ m s^{-1}, which corresponds to a circular orbit with a radius equal to the proper semimajor axis of (832) Karin. These nondimensional velocity components are denoted (v_r, v_t, v_z).

Neglecting first- and higher-order eccentricity and inclination terms, the Gauss equations (e.g., B. Bertotti et al. 2003) describe for each fragment the map between (v_r, v_t, v_z;$\omega_\star$, $f_\star$) and (δa, δe, $\delta \sin I$, $\delta\Omega$, $\delta\varpi$). This correspondence may be conveniently broken into three groups:

1. the transverse component v_t of the ejection velocity is directly connected with the change in semimajor axis δa as

$$\frac{\delta a}{a} = 2\, v_t, \tag{3}$$

2. a linear combination of the transverse v_t and radial v_r components of the ejection velocity determines changes in eccentricity δe and in longitude of perihelion $\delta\varpi$ expressed as a simple 2D rotation by $f_\star$

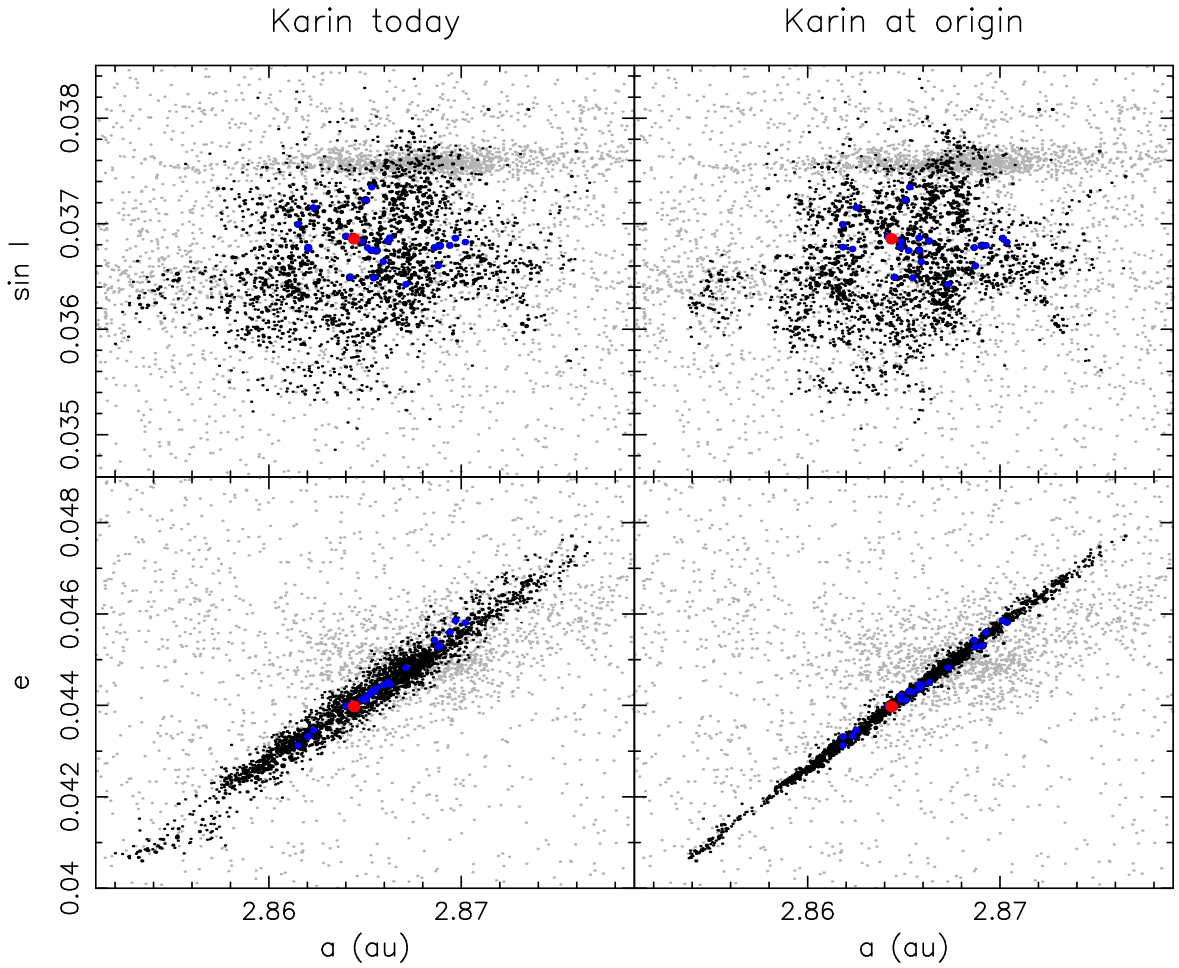

Figure 7. Karin family projected onto 2D planes of proper semimajor axis a at the abscissa, and proper sine of inclination $\sin I$ (top) and eccentricity e (bottom) at the ordinate. The largest body (832) Karin is shown by the red circle, and members with size $\gtrsim 3$ km are shown by blue symbols. The gray dots show unrelated background asteroids in the Koronis family. The left panels show the present-day configuration, and the right panels depict our reconstructed family at its formation $T = 5.72$ Mya. For that, we kept the $\sin I$ and e values constant, but shifted a values by $-\dot{a}\,T$, with drift rate $\dot{a}$ inferred from convergence of proper secular angles Ω and ϖ. The initial family shows two distinct features: (i) a more confined correlation in the (a, e) plane, and (ii) more focused filamentary structures in the (a, $\sin I$) plane (both predicted by D. Nesvorný et al. 2006a, using smoothed particle hydrodynamic, SPH, impact simulations).

$$\begin{pmatrix} \delta e \\ e\,\delta\varpi \end{pmatrix} = \begin{pmatrix} \cos f_\star & -\sin f_\star \\ \sin f_\star & \cos f_\star \end{pmatrix} \begin{pmatrix} 2\,v_t \\ -v_r \end{pmatrix}, \tag{4}$$

3. the out-of-plane velocity component v_z corresponds to the change in inclination $\delta \sin I$ and longitude of node $\delta\Omega$. It also has a straightforward interpretation in a 2D plane. Specifically, the pair ($\delta \sin I$, $\sin I \delta\Omega$) plays the role of the Cartesian axes, while the out-of-plane velocity v_z and angle $\omega_\star + f_\star$ function as polar coordinates

$$\delta \sin I = v_z \cos(\omega_\star + f_\star), \tag{5}$$

$$\sin I\ \delta\Omega = v_z \sin(\omega_\star + f_\star)\,. \tag{6}$$

In fact, an even simpler form of the velocity-to-orbital element relationships can be obtained by using nonsingular orbital elements $k = e\cos\varpi$, $h = e\sin\varpi$, $q = \sin I \cos\Omega$ and $p = \sin I \sin\Omega$, or their combination in complex variables $z = k + \imath\, h$ and $\zeta = q + \imath\, p$. Note that (z, ζ), in replacement of (e, I, Ω, ϖ), are (i) more appropriate for small eccentricity and inclination orbits and (ii) directly related to the construction of the proper orbital elements (e.g., Z. Knežević & A. Milani 2000; Z. Knežević et al. 2002; D. Nesvorný et al. 2024a).

Interestingly, the map between the variation of the orbital elements (δa, δz, $\delta\zeta$) and the imparted relative velocity (v_r, v_t, v_z) requires only a single parameter $F_\star = \varpi_\star + f_\star$, namely the true longitude in orbit of the parent body at the epoch of family formation. While Equation (3) still holds, the remaining system of equations is simplified to

$$\delta z = (2v_t - \imath\, v_r)\exp(\imath F_\star), \tag{7}$$

$$\delta\zeta = v_z \exp(\imath F_\star), \tag{8}$$

still valid to the zero order in orbital eccentricity and inclination.

We now aim to proceed in the opposite direction, namely, from differences in orbital elements to determining ejection velocities. Knowing the values of (δa, δe, $\delta \sin I$, $\delta\Omega$, $\delta\varpi$) or equivalently (δa, δz, $\delta\zeta$), we could—in an ideal world—use Equations (3), (7), and (8) to infer the relative velocity with which the body separated from (832) Karin. It is also worth noting that the angle $F_\star$ is identical for all fragments, which should further simplify the procedure.

For example, the real and imaginary parts of $\delta\zeta$, which we can construct from $\delta \sin I$ and $\sin I \delta\Omega$ of all family members,

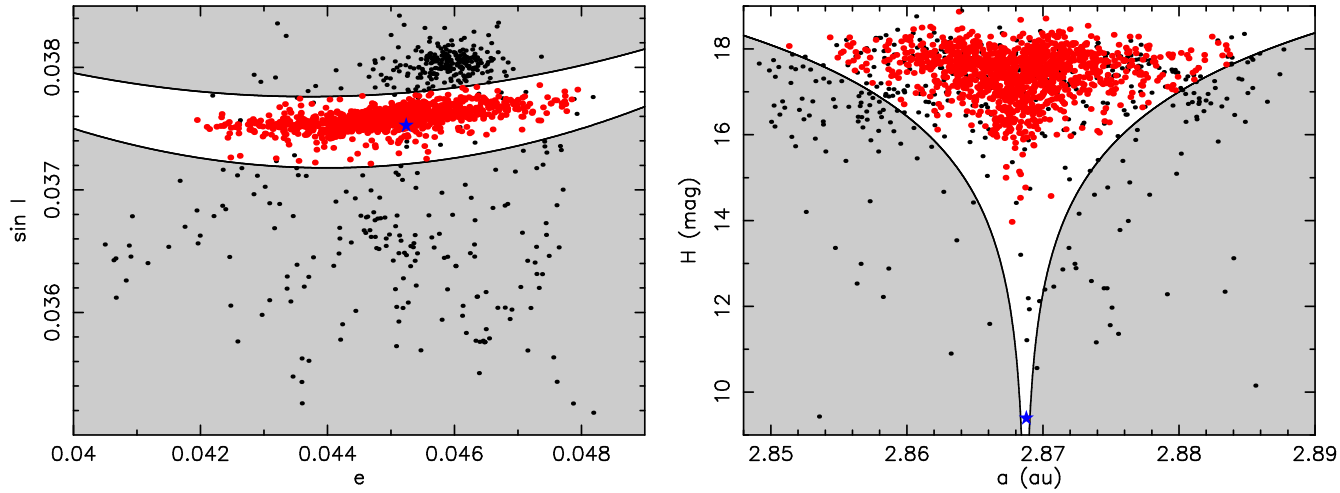

Figure 8. Pre-selection of Koronis2 family candidate members. Black symbols are all 1702 asteroids that remained in the HCM-identified Karin/Koronis2 family after Karin members were removed. A distinct property of Koronis2 real candidates, shown by the red symbols, is a tight confinement of their proper inclination values about $\sin I \simeq 0.0376$ (left panel). We used the two quadratic curves in the (e, $\sin I$) 2D space to characterize the zone of the Koronis2 family (bodies in the regions were eliminated). Asteroids at lower values of $\sin I$ are too far away in proper element space (median HCM distance from (158) Koronis of 60 m s^{-1}), and we consider them background members of the Koronis family. The tight cluster of asteroids at proper $e \simeq 0.0455$ and $\sin I \simeq 0.038$ are members of the interloping Koronis3 family (see Figure 1 in M. Brož et al. 2024; alternatively named the Kutaissi family by D. Nesvorný et al. 2026). The right panel presents the same data in the 2D projection of the (a, H) space. The proper semimajor axes of many large asteroids in the gray zone differ significantly from that of (158) Koronis (indicated by the blue star).

should fall along a single line in the respective complex plane with a phase given by $F_\star$. Similarly, with v_t components determined from the values of δa, the consistency of the configuration requires that the values of δz must map onto $2v_t - 1v_r$ using a simple rotation by the angle $-F_\star$ (Equation (8)). Along with identifying the values of $2v_t$ with $\delta a/a$ (Equation (3)), this transformation reveals the radial components v_r.

Although the procedure may seem straightforward, the main challenge lies in the fact that we do not know (δa, δz, $\delta\zeta$) of the osculating orbital elements when the family formed. Accordingly, we need to approximate them in some manner. We could use differences in the proper orbital elements (Δa, Δz, $\Delta\zeta$) at the moment of their convergence to represent (δa, δz, $\delta\zeta$). The issue is that as expected, they do not satisfy the conditions in Equations (7) and (8). Our attempts to adjust some of the parameters, such as the epoch T, the Yarkovsky drift $\dot{a}_j$, the proper frequencies[4] g_j and s_j, and their derivatives with respect the semimajor axis, unfortunately did not lead to a satisfactory solution.

We believe that the transformation between proper and osculating orbital elements introduces sufficient complexities to make the former unsuitable as substitutes for the latter in the above relations, particularly at the required meter-per-second precision for velocity components. In the Appendix, we investigate whether mean orbital elements, determined numerically for a sample of the largest Karin members identified above, might offer greater success in constraining the parameters of the initial velocity field.

[4] These parameters have formal uncertainties inherent to the procedure used to compute them. Their actual uncertainties, however, may be an order of magnitude larger. For example, test simulations reveal that gravitational perturbations of Karin family member orbits by Ceres, Pallas, and Vesta introduce noise in the proper elements equivalent to initial velocity components of approximately $\simeq$1.5 m s^{-1}, even over a timescale of just a few million years (see the Appendix and Figure 15).

3.2. Koronis2 Family

We now return to the population of the originally identified Karin/Koronis2 family, as determined using HCM in the 3D space of proper orbital elements. This cluster consists of 3863 asteroids, of which 2161 have been assigned to the Karin family (Section 3.1). The remaining 1702 asteroids represent potential members of the Koronis2 family. Since this family has also been proposed to be young (e.g., L. A. Molnar & M. J. Haegert 2009; M. Brož et al. 2024), we apply a similar convergence method to identify its members, as previously done for the Karin family, but now considering (158) Koronis as the largest body.

As with the second step of the Karin family analysis (Section 3.1.2), we first exclude obvious or suspected interlopers from the sample. This is necessary because convergence of secular nodes and perihelia alone is too weak of a criterion (any main belt asteroid can eventually converge to (158) Koronis in these two parameters alone). Membership in the Koronis2 family must also meet additional criteria related to proper element location and size, which essentially ensure that the relative velocity at convergence remains sufficiently small.

The tight clustering of the Koronis2 members in proper inclination proves beneficial in this regard. As a result, we analyzed the distribution of the 1702 candidate asteroids in the 2D projection of proper orbital elements e and $\sin I$, discarding those located too far from the main Koronis2 cluster (gray regions in the left panel of Figure 8). We chose this projection because it provides the best way to identify members of another interloping family, referred to as Koronis3 or Kutaissi by M. Brož et al. (2024) and D. Nesvorný et al. (2026): see the distinct cluster at about proper $e \simeq 0.0455$ and $\sin I \simeq 0.0376$. Asteroids on orbits with low values $\sin I$, defined as the lower gray region in the left panel, are dispersed, and their median HCM distance from (158) Koronis is $\sim$60 m s^{-1}. We consider them to be interloping objects, possibly members of the Koronis family.

We also removed several tens of asteroids that were too far from (158) Koronis in proper a for their absolute magnitude value H. This is the gray region shown in the right panel of Figure 8, delimited by curves showing $H = H_\star(a) = 5\log(|a - a_c|/c)$ with $a_c = 2.8687$ au and $c = 4.5 \times 10^{-6}$ au. The ejection speed needed to reach these curves from (158) Koronis would be $\geqslant 45$ m $^{-1}$ (see D. Vokrouhlický et al. 2006).

After completing this second step, the sample of potential Koronis2 members that satisfied the criteria in both the $(e, \sin I)$ and (a, H) spaces was reduced to 1250 asteroids. These are represented by red symbols in Figure 8. Admittedly, a small fraction of Koronis2 members near the borders of the elimination lines in Figure 8 may have been mistakenly excluded, but we believe this fraction is relatively small.

3.2.1. Nominal Convergence of Koronis2 Family

The largest member of the family, (158) Koronis, is the only asteroid with a sufficient observational dataset to allow for determination of its physical parameters. Lightcurve observations and stellar occultations have provided a well-constrained spin model, revealing a rotation period of 14.206 hr and pole orientation (30°,−64°) in ecliptic longitude and latitude (e.g., S. M. Slivan et al. 2003; J. Ďurech et al. 2011, respectively).

Additionally, occultation data analyzed in J. Ďurech et al. (2011) suggest a volume-equivalent size of 38 ± 5 km. This value is in conflict with the size 47.7 ± 0.6 km reported by the WISE team, perhaps due to albedo $p_V = 0.14 \pm 0.01$, unusually low compared to the mean albedo value of the Koronis family (e.g., J. R. Masiero et al. 2011). Further analyses of WISE's cryogenic and post-cryogenic phases resulted in somewhat smaller size estimates between approximately ≃31–39 km (J. R. Masiero et al. 2012, 2014), while other studies have reported sizes for Koronis within this interval as well (e.g., E. F. Tedesco et al. 2002; E. L. Ryan & C. E. Woodward 2010; F. Usui et al. 2011; V. Alí-Lagoa et al. 2018). Although there is some tension among these size estimates, the implications for our analysis are not particularly significant.

Here we adopt the 38 km diameter for (158) Koronis, partially because it is based on occultation data, but also because we suspect the anomalous WISE albedo may have been caused by the object's irregular shape. This size yields an estimated Yarkovsky drift rate of $\dot{a} \simeq -0.5 \times 10^{-5}$ au My^{-1}. This value is low compared to the drift rates of smaller members in the Koronis2 family, for which we conservatively assume $\dot{a}_{\max} = 4 \times 10^{-4}/D$ au My^{-1}. Note this is a slightly larger value than used in the case of the Karin family (Sections 3.1.1 and 3.1.2), since we aimed at giving somewhat larger parameter space to the Yarkovsky clones of the Koronis2 members to reach possibility of their convergence.

Following the approach used for the Karin family, we treat the drift rate $\dot{a}$ of (158) Koronis as fixed, while allowing adjustments for the drift rates of all other candidate members of the family. Although the WISE catalog provides size estimates for five of these smaller members, no additional information about their sizes or spin states is currently available. For the proper frequencies g_j and s_j, we use their nominal values and note that the majority of the population has uncertainties smaller than 2×10^{-4} arcseconds yr^{-1}, with only about 5% of the population showing larger uncertainties. Analyzing the nominal g_j and s_j values, we also determined the mean values of their gradient with respect to proper a, namely $(\partial s/\partial a) = -69\farcs8 \pm 0\farcs6$ yr^{-1} and $(\partial g/\partial a) = 86\farcs9 \pm 0\farcs9$ yr^{-1}.

The analysis of the past orbital convergence of Koronis2 members requires a fundamentally different approach than the one previously applied to the Karin family. In the case of the Karin family, even the nominal orbits, without any adjustment of free parameters (i.e., $\dot{a}_j = 0$ for all fragments), show a reasonable convergence of secular angles at a level of $\mathcal{C}' \simeq 15° - 20°$ near $T \simeq 5.8$ Myr (see already D. Nesvorný et al. 2002a). Adjusting $\dot{a}$ serves only to refine the convergence to a higher precision ($\mathcal{C}' \simeq 1°$), as first demonstrated by D. Nesvorný & W. F. Bottke (2004), but this process neither significantly alters the epoch T of convergence nor affects its uniqueness.

For the Koronis2 family, however, the situation is markedly different. The nominal orbits of its fragments do not show a clear convergence of nodes and perihelia. Achieving such convergence relies entirely on incorporating nonzero semimajor axis drifts $\dot{a}_j$. Moreover, the maximal drift rates for each Koronis2 candidate member impose a certain minimum value of T, the time of convergence in the past, for that particular body. Smaller drift rates, on the other hand, permit larger T values, typically spanning a wide range of past epochs. The intersection of these constraints across all candidate members still results in a substantial uncertainty regarding the family's age.

Complicating matters further, the convergence of the largest asteroids in the candidate list often pushes the epoch T to later times, potentially conflicting with the earlier convergence of smaller candidate asteroids. This discrepancy introduces ambiguity and necessitates subjective decisions about true membership in the Koronis2 family.

To highlight some of the challenges faced in determining the age of the Koronis2 family, we begin by testing the convergence of proper node and perihelion values independently. In our first trial, we looked at T between 7 and 15 Myr. We highlight two values: (i) $T = 7.6$ Myr, which was motivated by the work of (M. Brož et al. 2024), and (ii) $T = 10$ Myr (to illustrate the change of the results for older epochs). Our results are shown in Figure 9.

At both epochs shown, the majority of Koronis2 candidate members exhibit convergence of nodes and perihelia to (158) Koronis for reasonable semimajor axis drift-rate values. Interestingly, however, exceptions primarily occur for larger candidates, including asteroids (7719), (33143), and (40510). These three objects are likely members of the Karin family (Section 3.1.1) and thus may not pose a problem for determining the age of the Koronis2 family. Nevertheless, there are other potential Koronis2 members with $D > 2$ km, such as (15501), (55434), and (113021), whose proper nodes and perihelia also fail to converge to (158) Koronis at $T = 7.6$ Myr. Despite this, their proper $(a, e, \sin I)$ orbital elements and absolute magnitudes H place them well within the expected region of the Koronis2 family.

When T is shifted to 10 Myr, only (33143) and (40510) failed to achieve convergence of nodes and perihelia. Additionally, the panels in the right column of Figure 9 display the semimajor axis drift rates $\dot{a}_j$ required for the convergence of nodes and perihelia. While these values are often similar, they are not identical. In fact, achieving simultaneous convergence of both nodes and perihelia using

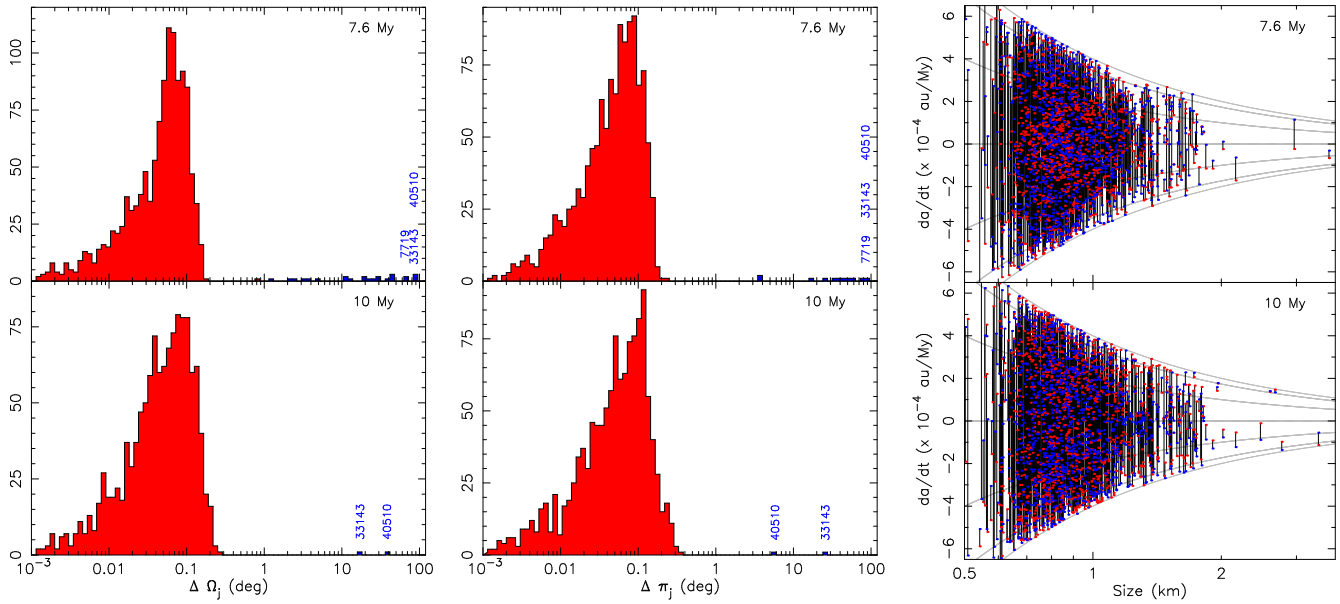

Figure 9. Left and middle panels: differential distribution of optimum $\Delta\Omega_j$ (left) and $\Delta\varpi_j$ (middle) for 1250 Koronis2 candidate members at two epochs in the past, 7.6 Myr (top) and 10 Myr (bottom). Optimization includes only adjustment of the semimajor axis drift rate $(da/dt)_j$ with the theoretical limit $\dot{a}_{\max} = \pm 4 \times 10^{-4}/D$ au My^{-1}. The bulk of mostly small asteroids converges well within the 1° threshold (red histogram). A certain number of larger asteroids do not converge, since their minimum $\Delta\Omega_j$ and $\Delta\varpi_j$ values remain large (tens of degrees; blue histogram). At 7.6 Myr, there are 23, resp. 11, such bodies including (7719), (33143), and (40510) that are also Karin family candidates (Section 3.1.1). The $D > 2$ km asteroids (15501), (55434), and (113021), however, also belong to this nonconvergent class. Shifting the epoch of origin to 10 Myr, only (33143) and (40510) remain in this class. Right panels: the adjusted $(da/dt)_j$ values for converging Koronis2 candidates at the respective epochs: red symbols are shown for convergence of nodal longitude, and blue symbols are shown for convergence of perihelion longitude (the values corresponding to the same asteroid are connected with black interval). The gray lines delimit the accepted drift rate values for a given size D (abscissa, logarithmic scale used as in Figure 6) with the characteristic $\propto 1/D$ dependence.

the same $\dot{a}_j$ value with our simplified method would require pushing T beyond 14 Myr.

Admittedly, determining a potential family age near or beyond 10 Myr may require more precise methods than simply relying on the convergence of proper secular angles. Small variations in the proper frequencies g_j and/or s_j, and particularly in their derivatives with respect to the semimajor axis, $(\partial g/\partial a)_j$ and $(\partial s/\partial a)_j$, which we assumed remain constant throughout the entire Koronis2 orbital region, could suggest that the dynamics are more complex than previously outlined. In order to test the effect of fine-tuning of $(\partial g/\partial a)_j$ and $(\partial s/\partial a)_j$ values, we let them to span a $\pm 1''$ yr^{-1} interval about the above-mentioned nominal values in the region of the Koronis2 family individually for each of the family candidates. Even with this extension of adjustable parameters, we obtained only 30% of converging orbits at the 7.6 Myr epoch in the past. A more detailed analysis of the Koronis2 family's age is therefore needed and deferred to future work.

For now, we assume that the pre-selected group of candidate asteroids represents genuine members of the Koronis2 family. The left panels of Figure 10 show these candidates projected onto 2D planes defined by proper semimajor axis versus eccentricity and proper semimajor axis versus sine of inclination, while the right panel displays their cumulative SFD. The blue and red lines represent variants that include or exclude asteroids (7719), (33143), and (40510), whose membership in the Koronis2 and Karin families remains ambiguous.

Similar to the case of the Karin family, the size distribution of the Koronis2 family in the 0.8–1.5 km range can be fit with a power law, $N(>D) \propto D^{-\alpha}$, where $\alpha = 3.95 \pm 0.01$. This value is only slightly shallower than that reported by M. Brož et al. (2024). If the slope exponent was steeper, the Koronis2 population could surpass that of the Karin family at sizes below a few hundred meters. Interestingly, this hypothesis can be directly tested with the forthcoming data from the Vera Rubin Observatory and NEO Surveyor.

3.3. Extrapolation of Karin and Koronis2 Observed Populations to Smaller Sizes

The cumulative SFD of multikilometer fragments in the Karin and Koronis2 families was found to follow a power law $N(>D) \propto D^{-\alpha}$, with $\alpha > 3$ (Figure 10). This trend cannot persist down to very small fragment sizes, as the total mass of the fragment population would quickly exceed the mass that could be plausibly be ejected from the parent body. This suggests that there must be at least one change in the slope exponent α at some subkilometer size. In fact, it is more likely that multiple such changes occur or that the power-law approximation is only locally valid and α varies as a more complex function of size D.

Here we briefly explore extrapolations of the observed SFDs in the identified Karin and Koronis2 families down to the meter-size range. We consider the simplest scenarios, namely broken power-law distributions with one or two transitions to different values of α.

Let us approximate the population of the largest family members with $N(>D) = (D_1/D)^{\alpha}$. For Karin and Koronis2 families, we find $D_1 \simeq 7.93$ km and $D_1 \simeq 4.4$ km, with the slope exponents having the values given above. Formally extending the SFD beyond D_1 to infinity, the collective volume of fragments

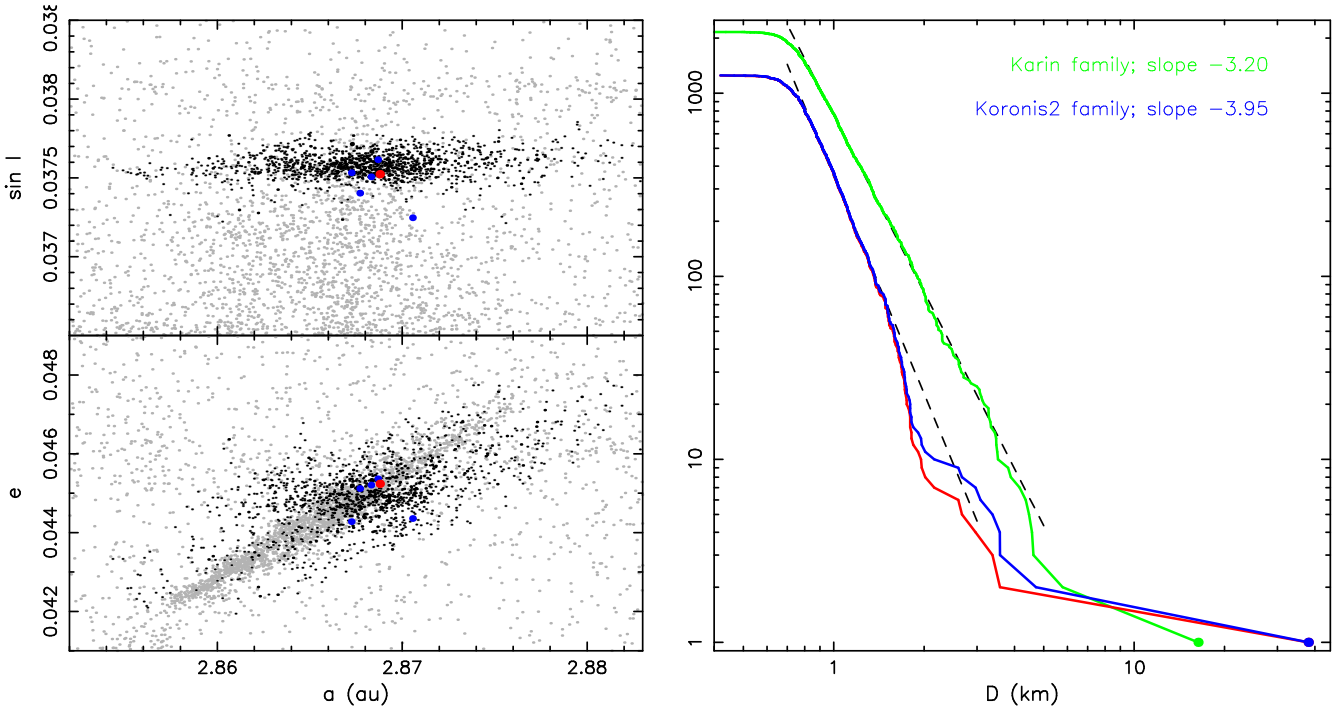

Figure 10. Left panels: Koronis2 family members (black symbols) projected onto 2D planes of proper semimajor axis a at the abscissa, and proper sine of inclination $\sin I$ (top) and eccentricity e (bottom) at the ordinate. The largest body (158) Koronis is shown by red circle, and members with size $\geqslant 3$ km are shown by blue symbols. The gray dots show unrelated background asteroids in the (old-)Koronis family, including the Karin cluster. Right panel: cumulative size distribution for 1250 members in our full identification of the Koronis2 family (blue) compared to the Karin family (green); the red curve shows a reduced version of Koronis2 without asteroids (7719), (33143), and (40510). The sizes of the four largest objects are from WISE observations, while those for the remaining members were determined from their absolute magnitude H and assumed albedo $p_V = 0.23$, the mean albedo value for the Koronis family from WISE data (J. R. Masiero et al. 2011, 2013). In between 0.8 and 1.5 km, the Koronis2 cumulative SFD is reasonably well matched by a power law $N(>D) \propto D^{-\alpha}$, with a slope index $\alpha = 3.95$ (dashed line). This slope is steeper than that of the Karin family over the same size range.

with a size larger than D is $V(>D) = V_1\,\phi_V(D;D_1,\,\alpha)$ with

$$\phi_V(D;\,D_1,\,\alpha) = \frac{\alpha}{\alpha-3}\left(\frac{D_1}{D}\right)^{\alpha-3}, \tag{9}$$

and the volume-equivalent size of spherical body they represent is $D_{\rm eff} = D_1\,\phi_V^{1/3}$. Here we see that D cannot follow this trend to small sizes, or both $V(>D)$ and $D_{\rm eff}$ would formally diverge in the limit $D \to 0$.

In order to keep the total volume of the fragments finite, we assume that the SFD becomes shallower below a certain break point $D_{\rm bp}$ with a power-law slope $\beta < 3$. It can be shown that the number of fragments with a size larger than $D < D_{\rm bp}$ is $N(>D) = N(>D_{\rm bp})\,\psi_N(D;D_{\rm bp},\,\alpha,\,\beta)$, and their volume is $V(>D) = V(>D_{\rm bp})\,\psi_V(D;D_{\rm bp},\,\alpha,\,\beta)$, where

$$\psi_N(D;\,D_{\rm bp},\,\alpha,\,\beta) = 1 + \frac{\alpha}{\beta}\left[\left(\frac{D_{\rm bp}}{D}\right)^{\beta} - 1\right], \tag{10}$$

$$\psi_V(D;\,D_{\rm bp},\,\alpha,\,\beta) = 1 + \frac{\alpha-3}{3-\beta}\left[1 - \left(\frac{D}{D_{\rm bp}}\right)^{3-\beta}\right]. \tag{11}$$

The model may be easily generalized to an arbitrary number of break points that separate different power-law segments of the SFD.

We now examine the hypothesis proposed in M. Brož et al. (2024), which suggests a link between the fragment populations of the Koronis2 (and Karin) families and the source of H-chondrite meteorites. This source was calibrated in that study to consist of approximately (1–2) $\times\ 10^{12}$ m sized main belt fragments. Our objective is to bridge this reference point with the observed kilometer-sized populations in the Karin and Koronis2 families using one or two break-point power-law approximations.

The constraints to be met are as follows. The modeling work of D. Nesvorný et al. (2006a) estimates the parent body of the Karin family had an original size of approximately 33 km. Given the current size of (832) Karin, about 16.3 km, this leaves an available fragment population volume equivalent to a sphere with an effective diameter of $D_{\rm eff} \simeq 31.6$ km.

However, the Karin family is also associated with the IRAS β dust band (see D. Nesvorný et al. 2003; D. Nesvorný et al. 2006b), so the fragment SFD must extend down to micrometer sizes. According to D. Nesvorný et al. (2006b), the volume of particles within the β dust band, spanning sizes from microns to centimeters, is equivalent to a sphere with a diameter of roughly 11 km. Even when accounting for the collisional evolution of these particles since the formation of the Karin family, as well as the uncalibrated segment of particles between a centimeter and a meter in size, we estimate that the total equivalent volume of fragments should not be greater than $\simeq$28–30 km.

Less information is available for the Koronis2 family, partly due to the uncertainty in the size, D_{158} of (158) Koronis itself. For now, we rely on the numerical results from D. D. Durda et al. (2007), who conducted an extensive suite of smoothed particle hydrodynamic (SPH) simulations involving impacts between projectiles and basaltic targets of $D = 100$ km. Here D. D. Durda et al. (2007) varied projectile sizes, impact geometries, and collision velocities to generate a database of synthetic fragment populations that could be compared to

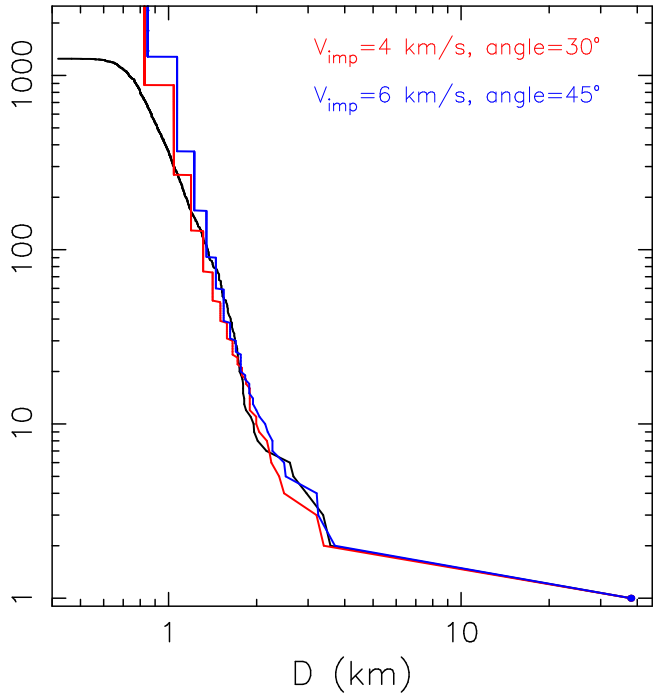

Figure 11. Comparison of the Koronis2 family population (black) with two results of basaltic asteroid breakup database obtained in D. D. Durda et al. (2007). In both cases, the size of the largest fragment was scaled to 38 km (assumed size of 158 Koronis), and the projectile size was 2.6 km. The small difference of predicted fragment populations is due to different impact angle, 30° (red) versus 45° (blue), and impact speed, 4 (red) vs. 6 km s^{-1} (blue). The equivalent volumes of the fragment populations are of spheres with diameters of 19 and 23 km, starting from the second-largest body.

observed asteroid families. Crucially, the simulated fragment populations conserved the total mass available in a given collision. By scaling these results to match the SFD of the largest fragments, presumably observationally complete, the simulations allow the total mass or equivalent volume of fragments to be calibrated.

Figure 11 presents two examples of synthetic fragment populations that closely match the Koronis2 SFD for fragments $\geqslant 1.1$ km in size. While the resolution of the D. D. Durda et al. (2007) simulations does not permit precise comparisons for fragments smaller than 1 km, the zero-order estimate of the total fragment volume remains valid (though we admit this conclusion needs to be verified by the future SPH simulations with much larger resolution).

The two simulations shown in Figure 11 correspond to equivalent fragment volumes associated with spheres of 19 and 23 km in diameter, starting from the second-largest object in the family. This estimate assumes a size of 38 km for (158) Koronis. We verified that assuming a larger size for (158) Koronis results in a correspondingly smaller total volume for Koronis2 fragments.

We first tested a single-break-point solution for the SFDs of the Karin and Koronis2 families in the range between meter and kilometer sizes. The results are shown in the upper two panels of Figure 12, where the axes represent combinations of ($D_{\rm bp}$, β) values that satisfy the required constraints.

We find that our solutions do a poor job of matching constraints, especially for the Koronis2 family: (i) $\beta > 3$ is consistently required, which shifts the problem of an overly massive SFD tail to sizes smaller than 1 m, and (ii) the minimum possible $D_{\rm eff}$ is $\simeq$29.8 km. Given our estimate of the total fragment population volume for Koronis2, equivalent to a sphere with a diameter of 19–23 km (starting from the second-largest body), the single-break-point power-law model is not viable.

This issue is mitigated under the assumption of a broken power-law model with two break points within the meter-to-kilometer size range, but at the cost of introducing more parameters and relying on less observational evidence. The bottom two panels of Figure 12 display possible combinations of ($D_{\rm bp1}$, β) values for the first segment, which must then be complemented by fine-tuned values of ($D_{\rm bp2}$, γ) for smaller fragment sizes. Under this two-break-point model, many solutions with $D_{\rm eff} < 23$ km become viable. Figure 13 presents exemplary test cases for both the single- and two-break-point solutions.

The key takeaway from our analysis is as follows. While high yields of small fragments from recent break-ups may be possible, the limited amount of source mass produced by a collision event imposes a significant constraint. Accordingly, extrapolations from the largest family members often result in an excessively large cumulative SFD of small fragments. If so, these solutions must be rejected.

Ideally, introducing "wiggles" into the fragment SFD could help address this problem. The issue is that such variations are not yet constrained by direct observational data. By incorporating these variations, one risks introducing a degree of arbitrariness into the results that could be problematic. For instance, it is plausible that all sorts of recent asteroid break-ups could produce similar quantities of small fragments if their ejecta SFDs were allowed to have flexible shapes.

4. Discussion and Conclusions

The new catalog of asteroid proper elements allowed us to substantially improve our knowledge of the Karin family. The principal results are as follows.

1. The up-to-date family contains 2161 members, nearly five times more than the previously published census.
2. The cumulative SFD of the Karin family between $\simeq$0.8 and $\simeq$3 km is well approximated by a power law with a slope 3.20 $\pm$ 0.01.
3. The excellent convergence of proper nodal and perihelion longitudes of Karin members, with a dispersion of $\simeq 1°$, can be achieved using reasonably constrained values of the semimajor axis drift rate (da/dt) caused by Yarkovsky thermal accelerations. For subkilometer Karin members, the da/dt values exhibit a bimodal distribution, with roughly symmetric peaks corresponding to about half of the maximum expected value for their size and a minimum near zero drift. This result provides strong evidence that the YORP effect has tilted the rotation pole directions of these asteroids away from the ecliptic plane. The maxima of the da/dt distribution are located near effective obliquities of approximately $\simeq 60°$ and $\simeq 120°$, but due to use of a simplified constant drift rate da/dt in our method, the exact obliquities of individual Karin members might be somewhat spread around these values.
4. The parameters suitable for achieving secular angle convergence enable us to estimate the initial configuration of the Karin family in the space of proper elements (a, e, $\sin I$). The results closely mimic data obtained

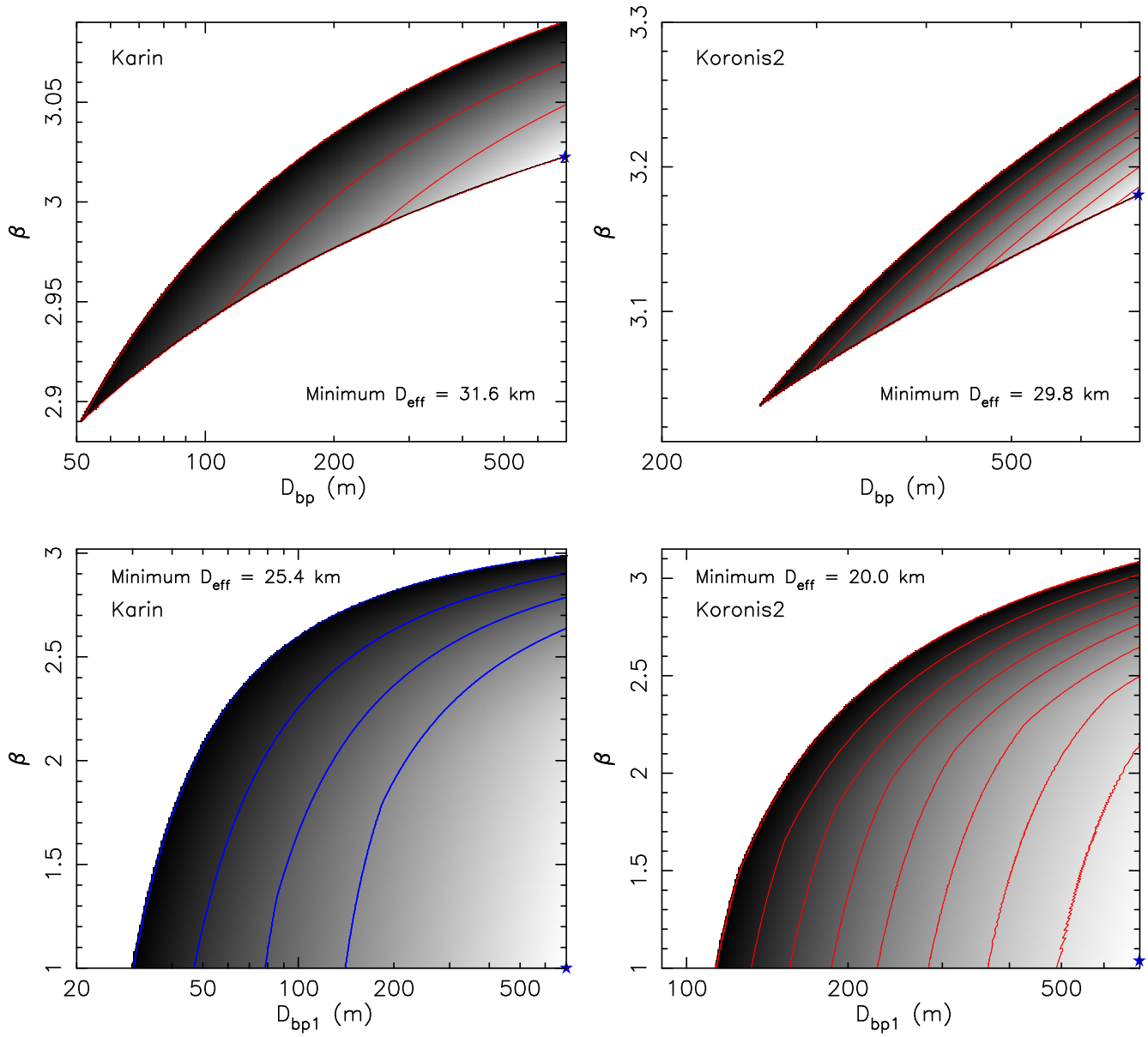

Figure 12. Top panels: Karin and Koronis2 extrapolated SFDs to meter size using a broken power law with a break point at $D_{\rm bp}$ (abscissa) and slope index β for $D < D_{\rm bp}$ (ordinate). The shaded area delimits possible solutions with the following constraints: (i) $N(>1\ {\rm m}) \geqslant 10^{11}$ and $D_{\rm eff} \leqslant 33$ km for the Karin family, (ii) and $N(>1\ {\rm m}) \geqslant 2\times10^{11}$ and $D_{\rm eff} \leqslant 33$ km for the Koronis2 family. The minimum possible solutions for $D_{\rm eff}$ are denoted by the blue star, and the values are given by the labels. The red isolines in the shaded region are for $D_{\rm eff} = 33$ km (at the upper zone of the admissible solution) decremented by 0.5 km. In both cases, the simple model with only one break point produces a tension by requiring too large minimum $D_{\rm eff}$ value. Bottom panels: the same as above, but now for a piecewise power-law SFD model with two break points. The abscissa shows the value of the first break point $D_{\rm bp1}$, and the ordinate is the slope β for $D_{\rm bp2} < D < D_{\rm bp1}$. The shaded area delimits possible solutions with the following constraints: (i) $N(>1\ {\rm m}) \geqslant 10^{11}$ and $D_{\rm eff} \leqslant 31$ km for the Karin family, and (ii) $N(>1\ {\rm m}) \geqslant 2\times10^{11}$ and $D_{\rm eff} \leqslant 28$ km for the Koronis2 family (in each of the cases, the location of the second break point $D_{\rm bp2}$ and the slope index γ for $D_{\rm bp2}$ are chosen to satisfy the constraints). The minimum possible solutions for $D_{\rm eff}$ are located by blue star, and the values are given by the labels. The blue isolines in the shaded region for Karin are for $D_{\rm eff} = 30$, 29 and 28 km solutions. The red isolines in the shaded region for Koronis2 are for $D_{\rm eff} = 28$ km (at the upper zone of the admissible solution) decremented by 1 km.

from numerical simulations of the parent asteroid's breakup that originally formed the Karin family. Considering the much larger number of Karin family members known today, it would be worthwhile to revisit and refine the breakup simulations in the near future.

5. We proposed a new metric function for orbital convergence, specifically designed for young asteroid families, which offers several advantages over the simple convergence of nodal and perihelion longitudes. This new approach eliminates singularities at zero eccentricity or inclination and directly relates to the properties of the initial ejection velocity field responsible for fragment dispersion. Additionally, we implemented an online determination of mean orbital elements and tested this framework on the Karin family. This analysis yielded an estimated age of 5.72 $\pm$ 0.09 Myr (95% C.L.) and expected ejection velocities of $\simeq$(10–20) m s^{-1} for kilometer size fragments.

An intriguing puzzle persists regarding the population of large Karin members. Specifically, three asteroids, (7719), (33143), and (40510), exhibit convergence with (832) Karin at

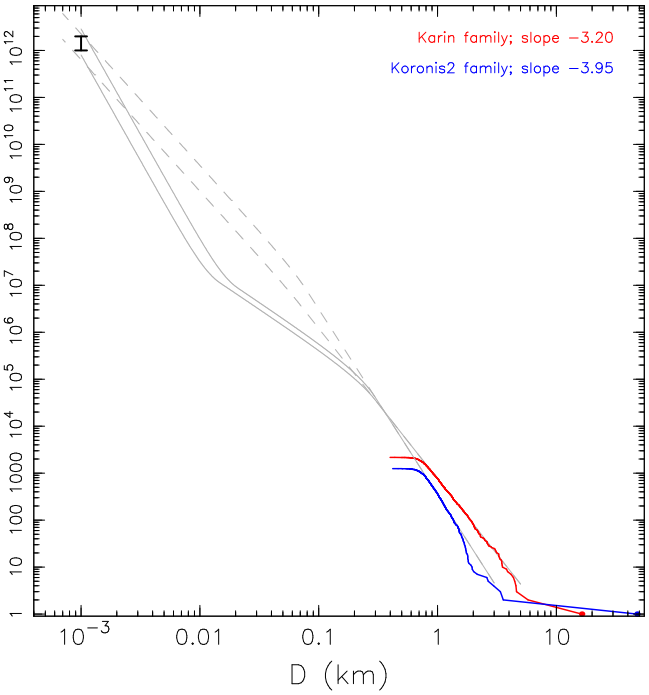

Figure 13. Linking the SFDs of the identified Koronis2 (blue) and Karin (red) families is essential to establish them as plausible sources of the IRAS 21 dust band (off-scale for size here) and H-chondrite meteorites. The slope exponents included in the labels correspond to the observed SFDs of the families down to ≃0.6–0.7 km. The solid gray lines represent extrapolations of the Koronis2 and Karin family SFDs, using two break points between power-law segments that satisfy the following criteria: (i) they reach the meter-sized population necessary to account for the observed flux of H-chondrite meteorites (black interval), and (ii) they maintain a reasonably small total volume, equivalent to a spherical body with a diameter of 24 km for the Koronis2 family and 27 km for the Karin family, respectively. In contrast, the previously suggested extrapolations with a single break point (illustrated by the dashed lines) consistently exceed the total available fragment volume (estimated here as 37 km for Koronis2 and 32 km for Karin). This analysis indicates that a wavy pattern in the SFD, spanning from meter-sized objects up to approximately 0.5 km, is necessary to reconcile the observations. On top of that, further breaks in the distribution would be needed below 1 m to link its value to the amount of dust needed in the dust band.

the formation epoch of the Karin family, but they also converge with (158) Koronis at epochs beyond 10 Myr, with the exception of (40510), which would require the Koronis2 family to have an age exceeding 15 Myr. Interestingly, determining their rotation poles could provide an effective means of distinguishing their family membership. For instance, if (7719) and (33143) belong to the Koronis2 family, and its age is ≃13 Myr, their pole obliquities would need to be ⩽40°. Conversely, if they are members of the Karin family, their rotation poles would likely align closer to the ecliptic plane. These predictions can be tested through an analysis of photometric observations.

Several upcoming small body surveys, such as the Vera Rubin Observatory and the NEO Surveyor mission, are poised to elevate our understanding of the Karin family to an entirely new level. For instance, the Vera Rubin Observatory is expected to complete the census of the main belt population down to $H \simeq 18.5$ (e.g., J. A. Kurlander et al. 2025). Assuming a geometric albedo of 0.23, this magnitude limit corresponds to an asteroid size of approximately 0.5 km. If the power-law slope of the SFD remains $\alpha \simeq 3.2$ all the way to this size limit, the observable population of the Karin family could increase to nearly 7000 objects. Alternatively, the SFD of the Karin family might start to bend shallower between approximately 0.3 and 0.5 km, and this feature could be detectable in the LSST data (note that existence of such a break point has recently been reported for very young families in the inner main belt; see D. Vokrouhlický et al. 2024).

Extending the analysis of the size dependence of mean da/dt values required for convergence (as shown in Figure 6) to sizes down to $D \simeq 0.5$ km might yield valuable insights into the degree of collisional activity and the characteristic YORP timescale for subkilometer asteroids in the main belt. For example, W. F. Bottke et al. (2005) predicted a collisional lifetime of approximately 100 Myr for a 0.5 km asteroid. Statistically, this suggests that around ≃6% of the smallest known Karin members should have undergone a catastrophic collision. Similarly, the calibration of mean YORP strengths by V. Carruba et al. (2016) for multikilometer Karin members indicates that the YORP timescale for 0.5 km objects should be as short as ≃15 Myr. The combined effects of these two processes will largely determine the degree of polarization of da/dt in Figure 6 at such small sizes.

Another approach to estimate the average strength of the YORP effect would be to determine the fraction of asteroid pairs among the Karin family members (e.g., D. Vokrouhlický & D. Nesvorný 2008). This is because such pairs are predominantly formed through YORP-driven rotational fission of their parent asteroids (e.g., P. Pravec et al. 2010). While we did not conduct a systematic search for asteroid pairs within the current Karin population in this study, we note one remarkable example: asteroids (82780) 2001 QF18 and (604365) 2015 PO96. These two objects appear to form a primary–secondary pair, and are estimated to be ≃100 kyr old. The primary is ≃2.6 km in size, while the secondary has an approximate size of 1 km. Beyond this, no additional data on their physical properties, such as rotational periods, are currently available. Future observations from upcoming large-scale surveys, which will greatly expand the known Karin population, are expected to reveal many more such cases.

The accurate determination of the Karin family has allowed us to better isolate the candidate population of the partially overlapping Koronis2 family compared to previous studies. The kilometer-sized population of the Koronis2 family exhibits a very steep SFD, approximated by a power law with a cumulative slope of 3.95 ± 0.01. We attempted to determine the age of the Koronis2 family using the simple convergence of proper node and perihelion longitudes with (158) Koronis. Unfortunately, the situation is more complex than in the case of the Karin family. While the age of 7.6 Myr proposed by M. Brož et al. (2024) is plausible, it is challenged by the apparent lack of convergence among some large candidate members.

In our analysis, this issue can be resolved if the Koronis2 family is assumed to be older than 7.6 Myr. If so, the Koronis2 family may no longer be a good candidate to explain the large fraction of H chondrites with cosmic-ray exposure ages near this age (e.g., K. Marti & T. Graf 1992; T. Graf & K. Marti 1995). Alternatively, the limitations of our methodology could mean that the Koronis2 age must be determined through direct numerical simulations. When this is revisited in the future, we recommend using the new convergence metrics outlined in the Appendix.

With our updated membership for the Karin and Koronis2 families, which are presumed complete down to approximately 1 km in size, we briefly revisited extrapolations to the meter-size population, particularly in the context of their relevance as meteorite sources. We find that the threshold levels established in M. Brož et al. (2024) can be met, but achieving this feat is challenging, if not impossible, under the simplest assumption of a broken power law with two segments of constant slope indices and a single break point. Such models tend to systematically predict excessively large fragment populations. Although the issue can be mitigated by introducing additional power-law segments, this approach introduces arbitrary elements into the models, making the proposed solutions less compelling.

Acknowledgments

The authors thank Miroslav Brož for helpful discussions and the referee, Bojan Novaković, for providing suggestions that significantly improved the original version of this paper. The work of D.V. was supported by the Czech Science Foundation through grant 25-16507S. The work of D.N. and W.B. was supported by the NASA's solar system Workings program through grant 80NSSC21K1829.

Appendix
Convergence of Large Karin Members in Mean Orbital Elements

In this appendix, we explore the possibility of using mean, instead of proper, orbital elements for convergence studies of young asteroids families and illustrate our approach in the case of the Karin family. While not new in this respect (see, e.g., B. Novaković et al. 2012, 2014), our goal is to (i) remove singular behavior of the secular angles when eccentricity or inclination become very small, and (ii) achieve a stronger link to the initial configuration of the family than provided by simple convergence of the secular angles and to obtain higher precision in its reconstruction (Section 3.1.3). These high ambitions require one to switch from an analytical to a numerical approach to the problem. Yet, results obtained in Section 3.1 provide us with important initial information. This includes: (i) identification of Karin family members, and (ii) pre-constrained values of the optimum model parameters that point to the family origin at $T \simeq 5.72$ Myr (such as the $\dot{a}_j$ of each of the family asteroids).

Numerical integrator. The numerical simulations were performed using the well-tested integration package `swift`[5] that we complemented with two extensions. The first emulates the Yarkovsky effect using a simple along-track acceleration that results in the expected secular semimajor axis drift $\dot{a}$. This part has been used and tested repeatedly in a number of our previous studies of asteroid families (e.g., D. Vokrouhlický et al. 2006). The new feature is the computation of the mean orbital elements.[6] We adopted the AAAB sequence of low-frequency filters described and tested in T. R. Quinn et al. (1991) and implemented them as a tool into the swift package. We used a 6 day time step and 36 day sampling frequency of the bottom A-filter. As suggested in T. R. Quinn et al. (1991), we used a shift factor of 10 before applying the next filter in the hierarchy. With that scheme applied, the signal with periods less than $\simeq$660 yr is suppressed with a factor better than 10^{-4}, while the secular variations of the orbital elements with periods larger than $\simeq$2 kyr are effectively preserved. This is an excellent realization of the numerical transformation between the osculating and mean orbital elements. The initial heliocentric state vectors for all planets and asteroids were obtained from the JPL Horizons website and correspond to the initial epoch MJD 60800. They were given in the ecliptic system of J2000.0, but before the propagation, we rotated them into the invariable (Laplacian) system. In order to represent backward orbital evolution, we inverted orbital velocities and the semimajor axis drift rates $\dot{a}$ for all asteroids. We used a priori values from the convergence solution in proper orbital elements (Section 3.1), but allowed slight adjustments within $\pm 2 \times 10^{-5}$ au My^{-1}.

Target function. Since the mean orbital elements contain more detailed information about the orbital evolution than the proper elements used in the main text (in particular, the mean eccentricities e and inclinations I are not constant), the target function (Equation (2)) for the minimization algorithm to track the family origin should be replaced with an appropriately more complex form, now depending also on the behavior of e and I. Equations (7) and (8), characterizing the change in the orbital elements at the origin and its direct relation to the velocity field, provide the basis. Since the target function must be positive definite, we use

$$\mathcal{C}^2(T) = \mathcal{C}_z^2 + \mathcal{C}_\zeta^2 = \sum_{j=1}^{N} [\Delta z_j \, \Delta \bar{z}_j + \Delta \zeta_j \, \Delta \bar{\zeta}_j], \qquad \text{(A1)}$$

where $\Delta z = \Delta k + \imath \, \Delta h$ and $\Delta \zeta = \Delta q + \imath \, \Delta p$ are the numerically inferred differences of the mean orbital elements with respect to (832) Karin (the overbar means a complex conjugate quantity). If the correspondence to the ejection velocities was the same as for the osculating orbital elements, the target function (A1) would have the following interpretation in the velocity field components: $\mathcal{C}^2 = \sum_{j=1}^{N} [v_r^2 + 4 v_t^2 + v_z^2]_j$ valid to the zero order in orbital eccentricity e.[7] Similarly, the $\mathcal{C}_z^2 = \sum_{j=1}^{N} [v_r^2 + 4 v_t^2]$ and $\mathcal{C}_\zeta^2 = \sum_{j=1}^{N} v_z^2$ parts would characterize contributions of the in-plane and out-of-plane velocity components. Analyzing the two parts separately offers the possibility—at least in principle—to probe various coarse hypotheses about the ejection velocity field. For example, consider that fragments were ejected with a characteristic velocity v and directed uniformly in conus with an opening angle $\theta_\star$ in the out-of-plane direction. Then, $\mathcal{C}_z^2 = \frac{5}{3} v^2 \left(1 - \frac{1}{2} \phi_\star\right)$ and $\mathcal{C}_\zeta^2 = \frac{1}{2} v^2 (1 + \phi_\star)$ with $\phi_\star = \cos\theta_\star (1 + \cos\theta_\star)$. If the conus is directed along the transverse direction in the orbital plane, the weight changes in favor of $\mathcal{C}_z^2$, and one has $\mathcal{C}_z^2 = \frac{5}{3} v^2 \left(1 + \frac{7}{25} \phi_\star\right)$ and $\mathcal{C}_\zeta^2 = \frac{1}{3} v^2 \left(1 - \frac{1}{2} \phi_\star\right)$. An isotropic ejection field, $\theta_\star = \pi$, yields in both cases $\mathcal{C}_z^2 = 5 \, \mathcal{C}_\zeta^2$, and the

[5] H. F. Levison & M. J. Duncan (1994) and http://www.boulder.swri.edu/~hal/swift.html.

[6] See also an extensive software package by Mira Brož available at GitHub, which also includes digital filtering and many more options (https://github.com/miroslavbroz/swift_rmvs3_fp_ye_yorp).

[7] Developing $\mathcal{C}^2$ to the first power in orbital eccentricity, and dropping terms depending on orbital true anomaly (information not accessible by the mean orbital elements), we obtain $\mathcal{C}^2 = \sum_{j=1}^{N} \left[v_r^2 + v_r v_t \, h_\star + 4 v_t^2 \left(1 - \frac{1}{2} k_\star\right) + v_z^2 \right]_j$, where $k_\star$ and $h_\star$ are the nonsingular variables of the reference orbit (such as 832 Karin).

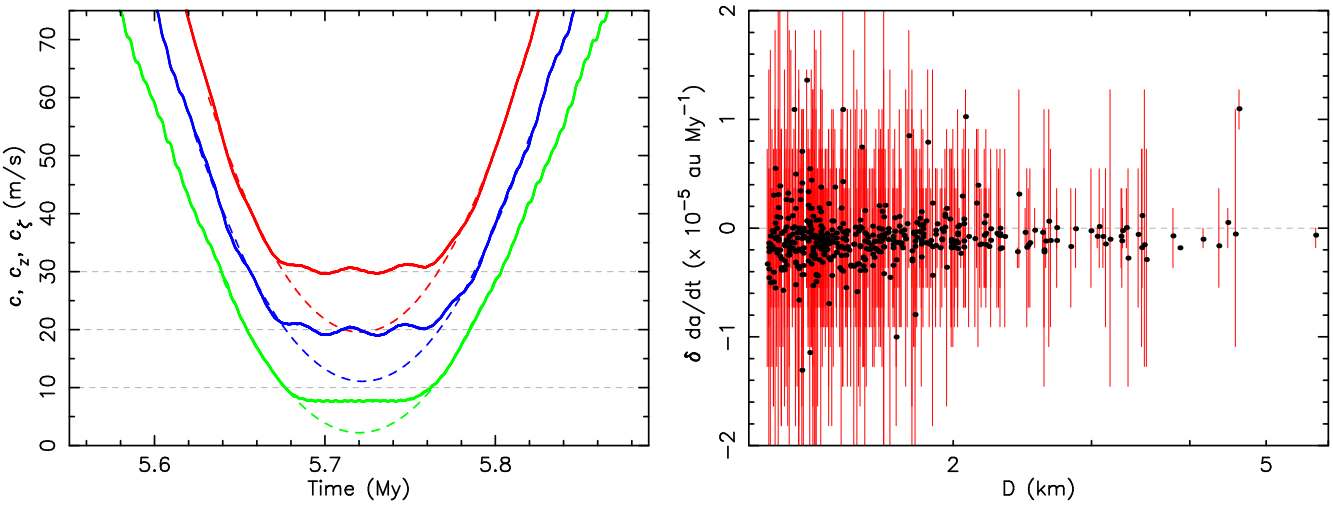

Figure 14. Convergence of orbits of the 450 largest Karin family members using mean orbital elements. The left panel shows quantitative indicators of the success expressed using metrics in Equation (A1) normalized to one converging orbit and given in velocity units: (i) $\bar{\mathcal{C}}$ combining contribution from all initial velocity components (red curve), (ii) $\bar{\mathcal{C}}_z$ depending only the in-plane radial and transverse ejection velocity components (blue curve), and (iii) $\bar{\mathcal{C}}_\zeta$ depending only on the out-of-plane ejection velocity component (green curve). The horizontal dashed lines provide reference levels of 10, 20, and 30 m s^{-1}. Perturbations by massive bodies in the main belt, Ceres, Pallas, or Vesta (not included in the simulation) prevent minimum values at $T \simeq 5.72$ Myr from decreasing deeper along the dashed lines, which represent a quadratic fit of the wings of the functions. The wavy pattern in $\bar{\mathcal{C}}_z$, reflected also on $\bar{\mathcal{C}}$, is likely produced by perihelion precession of Karin's orbit (see the main text). The right panel shows slight adjustments of the semimajor axis drift rates $\dot{a}$ for individual orbits compared to their a priori solutions from the convergence of the orbits using only proper node and perihelion values (shown in Figures 3 and 6) as a function the asteroid size D. These corrections are very small, <10% of the a priori values. The black symbols are the mean, and red vertical bar is the range between minimum and maximum values, of $\dot{a}$-corrections for epochs T between 5.69 and 5.74 Myr.

same result is also obtained for the hemispheric ejection fields, $\theta_\star = \pi/2$. This degeneracy is caused by only quadratic velocity-component contribution in $\mathcal{C}^2$. For the sake of reporting our results in units of velocity, we also define $\bar{\mathcal{C}} = V_0\sqrt{\mathcal{C}^2/N}$, $\bar{\mathcal{C}}_z = V_0\sqrt{\mathcal{C}_z^2/N}$ and $\bar{\mathcal{C}}_\zeta = V_0\sqrt{\mathcal{C}_\zeta^2/N}$ with $V_0 = 17600$ m s^{-1}.

Preliminary results. Figure 14 shows the results for 450 largest members in the Karin family. The left panel expresses their convergence using the new metrics $\bar{\mathcal{C}}$ in (A1), and the related parts $\bar{\mathcal{C}}_z$ and $\bar{\mathcal{C}}_\zeta$ depending on the in-plane and out-of-plane ejection velocity components. They can be directly compared with $\mathcal{C}'$ in Figure 2 since at each past epoch T, we adjusted individual drift rate values $\dot{a}_j$ to achieve the optimum convergence level. The minima of all metric functions are now appreciably narrower in T and the expression of a higher-fidelity convergence procedure. However, at their minima, none of the $\bar{\mathcal{C}}$-functions are matched by a quadratic function in T as expected (see the fits shown by the dashed lines). We believe that this behavior has to do with perturbation by massive objects in the main belt, dominantly Ceres and Pallas, which are not included in our simulation, yet they affected the present-day orbits of Karin members. In the next appendix section, we briefly examine their expected level and conclude that it may easily explain the few meter-per-second deficiency in minima seen in Figure 14. If we were to consider the ideal quadratic profile from the $\bar{\mathcal{C}}_\zeta$ component and $\simeq$5 m s^{-1} noise (at the level of the minimum deficiency), the formal Gaussian statistics would set the 95% C.L. for the Karin family age solution at 5.72 $\pm$ 0.09 Myr. The wavy pattern at the minima of the $\bar{\mathcal{C}}$ functions is an interesting characteristic, most likely an expression of first order in e terms (see footnote 3). Analyzing its amplitude may provide further information about the statistical distribution of the radial and transverse ejection velocity fields. The right panel of Figure 14 shows the range of adjustments $\dot{a}$ required to achieve the best convergence in mean orbital elements compared to those following from proper orbital elements (Section 3.1). These corrections are very small and only weakly dependent on the size D, indicating that the solution followed from the convergence of the proper secular angles is already a very good approximation.

The convergence approach in the space of mean orbital elements briefly outlined in this appendix seems to us a promising novel tool that directly reaches quantitative aspects of the initial ejection field of fragments in the family. Our goal here was to introduce it and use it to justify results in the main body of the paper, but not to elaborate on its details. We postpone this work to future publications.

A.1. Perturbations from Massive Bodies in the Main Belt

In order to probe the role of the gravitational perturbations by most massive bodies in the main belt in the Karin and Koronis2 orbital zone, we conducted the following experiment. We selected the largest 252 asteroids in the Karin family, roughly uniformly distributed in proper a and e values. We set their semimajor axis drift rates to zero and propagated their orbit for 10 Myr backward in time. If only planets were included, the mean semimajor axes a of the family members should have been constant (except for resonant effects, which are tiny in this orbital region). In addition to planets, we also included three perturbers embedded in the main belt, namely (1) Ceres, (2) Pallas, and (4) Vesta (CPV), accounting for more than 50% of its mass. While less massive than planets, the nature of their gravitational influence on members in the Karin family is significant and consists of two distinct processes: (i) a cumulative effect of distant encounters resulting in quasi-random walk in the orbital space, and (ii) stronger, but less frequent, perturbations due to deep close encounters. We illustrate their effects on the evolution of the mean semimajor axes of our sample of Karin members. To that end, we

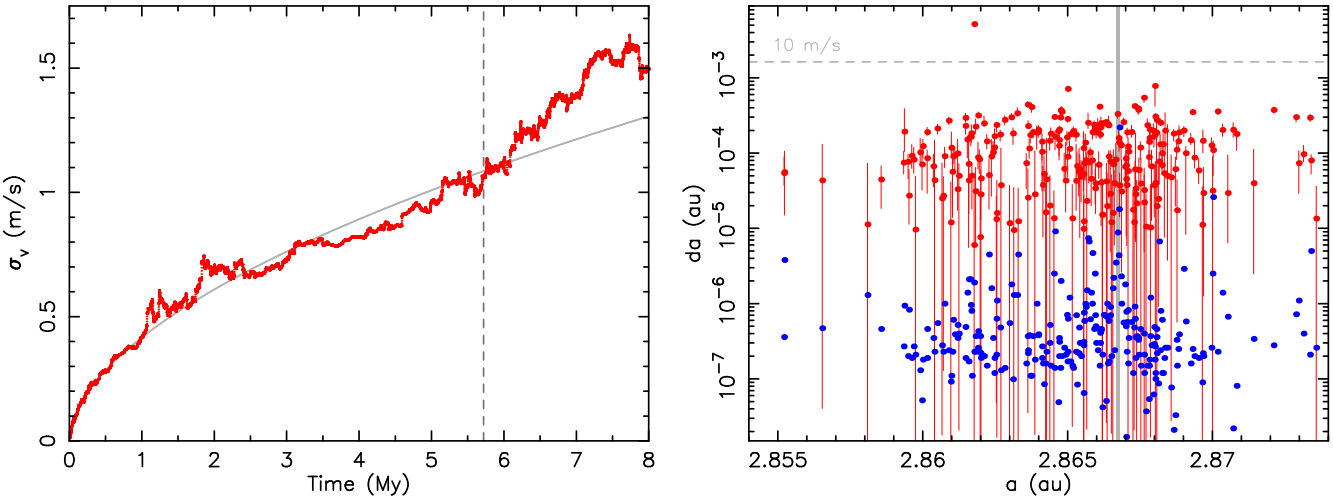

Figure 15. The effect of massive bodies in the asteroid belt—(1) Ceres, (2) Pallas, and (4) Vesta (CPV)—on mean semimajor axis of members in the Karin family. Left panel: growth of the semimajor axis dispersion expressed by $\sigma_a^2(T) = \langle [a(T) - a(0)]^2 \rangle$ with time T translated to characteristic velocity perturbation using $\sigma_v = V_0\, \sigma_a/a_0$ ($V_0 = 17{,}600$ m s^{-1} and $a_0 = 2.865$ au). An approximate power-law fit $\sigma_v \propto T^{0.66}$ is shown by the gray line. Orbits that underwent only distant encounters with CPV contribute to this statistics, as those suffering deep encounters do not obey statistical properties of a quasi-random walk. The vertical dashed line marks the 5.72 Myr age of the Karin family. Right panel: the change in the mean semimajor axis $da(T) = |a(T) - a(0)|$ for T in between 5.5 and 6 Myr for orbits of 252 largest members in the Karin family. The red symbols are the median, and the lines show the range of minimum to maximum value (the vertical gray line denotes location of a 3-body mean motion resonance 4λ–$13\lambda_J + 8\lambda_S + \varpi$ with Jupiter and Saturn; see T. Gallardo 2014). The blue symbols are formal standard deviations of the proper elements from D. Nesvorný et al. (2024a). The dashed horizontal line corresponds to an equivalent velocity kick of 10 m s^{-1}. Orbits contributing above this threshold (one out of 252 over 6 Myr) imply deep encounters with CPV.

determine the change in the mean semimajor axis $\delta a_j(T) = a_j(T) - a_j(0)$ for each asteroid orbit and past epoch T, and from these values, we compute the characteristic dispersion $\sigma_a^2(T) = \sum_j \delta a_j^2/N$ (which can also be expressed in terms of velocity $\sigma_v = V_0\, \sigma_a/a_0$, where $V_0 = 17{,}600$ m s^{-1} and $a_0 = 2.865$ au). The sum goes over $j = 1, \ldots, N$, where N is the subsample of bodies undergoing only distant encounters (process (i) above). We monitor the effects of deep encounters separately, identifying them with $|\delta a_j| > 2 \times 10^{-3}$ au.

Figure 15 summarizes the results of our simulation. The left panel shows the growth of the dispersion $\sigma_v(T)$ in the sample of orbits avoiding deep encounters with CPV. As already found in D. Nesvorný et al. (2002b; see also V. Carruba et al. 2003), $\sigma_v(T) \propto T^\beta$ with $\beta \simeq 0.66$, slightly larger than the 0.5 expected for a random-walk process. This is likely because of the correlated or repeated encounters with CPV during favorable orbital alignments. The right panel shows the accumulated values $\delta a_j(T)$ for $T \in (5.5, 6)$ Myr (red symbols). The majority of the data correspond to the population of orbits with only distant CPV encounter history, for which $\delta a_j \simeq (2\text{–}3) \times 10^{-4}$ au is appreciably greater than the formal uncertainty of the proper a values determined in a dynamical model with only planetary effects included (blue symbols). We found that one orbit of the 252 sample had a deep encounter with CPV within the 6 Myr time interval. This case, with $\delta a > 2 \times 10^{-3}$ au, is distinct from the other orbits.

The takeaway message from our simulation is as follows. Perturbations from CPV, and other massive asteroids in the main belt, impose a noise in the orbital convergence efforts of young families. In the case of the Karin family, it is of the order of meters per second in each of the ejection velocity components, explaining the difference between the ideal minima and observed "stalled" minima of the $\bar{\mathcal{C}}$-metric functions shown in the left panel of Figure 14. Additionally, a few percent of Karin family objects might have suffered significant orbital change due to deep encounters with CPV that would even prevent their identification as its members from today's orbits.

ORCID iDs

David Vokrouhlický https://orcid.org/0000-0002-6034-5452
David Nesvorný https://orcid.org/0000-0002-4547-4301
William F. Bottke https://orcid.org/0000-0002-1804-7814

References

Alí-Lagoa, V., Müller, T. G., Usui, F., & Hasegawa, S. 2018, A&A, 612, A85
Bertotti, B., Farinella, P., & Vokrouhlický, D. 2003, Physics of the Solar System - Dynamics and Evolution, Space Physics, and Spacetime Structure (Kluwer)
Bottke, W. F., Durda, D. D., Nesvorný, D., et al. 2005, Icar, 179, 63
Brož, M., Vernazza, P., Marsset, M., et al. 2024, Natur, 634, 566
Carruba, V., Burns, J. A., Bottke, W., & Nesvorný, D. 2003, Icar, 162, 308
Carruba, V., Nesvorný, D., & Vokrouhlický, D. 2016, AJ, 151, 164
Durda, D. D., Bottke, W. F., Nesvorný, D., et al. 2007, Icar, 186, 498
Ďurech, J., Kaasalainen, M., Herald, D., et al. 2011, Icar, 214, 652
Gallardo, T. 2014, Icar, 231, 273
Graf, T., & Marti, K. 1995, JGR, 100, 21247
Knežević, Z., Lemaître, A., & Milani, A. 2002, in Asteroids III, ed. W. F. Bottke, Jr et al. (Univ. Arizona Press), 603
Knežević, Z., & Milani, A. 2000, CeMDA, 78, 17
Kurlander, J. A., Bernardinelli, P. H., Schwamb, M. E., et al. 2025, AJ, 170, 99
Levison, H. F., & Duncan, M. J. 1994, Icar, 108, 18
Marti, K., & Graf, T. 1992, AREPS, 20, 221
Masiero, J. R., DeMeo, F. E., Kasuga, T., & Parker, A. H. 2015, in Asteroids IV, ed. P. Michel, F. E. DeMeo, & W. F. Bottke (Univ. Arizona Press), 323
Masiero, J. R., Grav, T., Mainzer, A. K., et al. 2014, ApJ, 791, 121
Masiero, J. R., Mainzer, A. K., Bauer, J. M., et al. 2013, ApJ, 770, 7
Masiero, J. R., Mainzer, A. K., Grav, T., et al. 2011, ApJ, 741, 68
Masiero, J. R., Mainzer, A. K., Grav, T., et al. 2012, ApJL, 759, L8
Milani, A., Cellino, A., Knežević, Z., et al. 2014, Icar, 239, 46
Molnar, L. A., & Haegert, M. J. 2009, AAS/DPS Meeting, 41, 27.05
Nesvorný, D., & Bottke, W. F. 2004, Icar, 170, 324
Nesvorný, D., Bottke, W. F., Jr, Dones, L., & Levison, H. F. 2002a, Natur, 417, 720
Nesvorný, D., Bottke, W. F., Levison, H. F., & Dones, L. 2003, ApJ, 591, 486

Nesvorný, D., Brož, M., & Carruba, V. 2015, in Asteroids IV, ed. P. Michel, F. E. DeMeo, & W. F. Bottke (Univ. Arizona Press), 297
Nesvorný, D., Enke, B. L., Bottke, W. F., et al. 2006a, Icar, 183, 296
Nesvorný, D., Morbidelli, A., Vokrouhlický, D., Bottke, W. F., & Brož, M. 2002b, Icar, 157, 155
Nesvorný, D., Roig, F., Vokrouhlický, D., & Brož, M. 2024a, ApJS, 274, 25
Nesvorný, D., Vokrouhlický, D., Bottke, W. F., & Sykes, M. 2006b, Icar, 181, 107
Nesvorný, D., Vokrouhlický, D., Brož, M., & Roig, F. V. 2026, Icar, 443, 116768
Nesvorný, D., Vokrouhlický, D., Shelly, F., et al. 2024b, Icar, 411, 115922
Novaković, B., Hsieh, H. H., & Cellino, A. 2012, MNRAS, 424, 1432
Novaković, B., Hsieh, H. H., Cellino, A., Micheli, M., & Pedani, M. 2014, Icar, 231, 300
Novaković, B., Vokrouhlický, D., Spoto, F., & Nesvorný, D. 2022, CeMDA, 134, 34
Pravec, P., Vokrouhlický, D., Polishook, D., et al. 2010, Natur, 466, 1085
Press, W. H., Teukolsky, S. A., Vetterling, W. T., & Flannery, B. P. 2007, Numerical Recipes: The Art of Scientific Computing (Cambridge Univ. Press)
Quinn, T. R., Tremaine, S., & Duncan, M. 1991, AJ, 101, 2287
Ryan, E. L., & Woodward, C. E. 2010, AJ, 140, 933
Scheeres, D. J., Britt, D., Carry, B., & Holsapple, K. A. 2015, in Asteroids IV, ed. P. Michel, F. E. DeMeo, & W. F. Bottke (Univ. Arizona Press), 745
Slivan, S. M., Binzel, R. P., Crespo da Silva, L. D., et al. 2003, Icar, 162, 285
Slivan, S. M., & Molnar, L. A. 2012, Icar, 220, 1097
Tedesco, E. F., Noah, P. V., Noah, M., & Price, S. D. 2002, AJ, 123, 1056
Usui, F., Kuroda, D., Müller, T. G., et al. 2011, PASJ, 63, 1117
Vokrouhlický, D. 1998, A&A, 335, 1093
Vokrouhlický, D., Bottke, W. F., Chesley, S. R., Scheeres, D. J., & Statler, T. S. 2015, in Asteroids IV, ed. P. Michel, F. E. DeMeo, & W. F. Bottke (Univ. Arizona Press), 509
Vokrouhlický, D., Brož, M., Bottke, W. F., Nesvorný, D., & Morbidelli, A. 2006, Icar, 182, 118
Vokrouhlický, D., & Nesvorný, D. 2008, AJ, 136, 280
Vokrouhlický, D., Nesvorný, D., Brož, M., & Bottke, W. F. 2024, A&A, 681, A23
Zappalà, V., Cellino, A., Farinella, P., & Knežević, Z. 1990, AJ, 100, 2030